AGU PUBLICATIONS

Geochemistry, Geophysics, Geosystems

RESEARCH ARTICLE
10.1002/2016GC006617

Influence of mantle flow on the drainage of eastern Australia since the Jurassic Period

T. Salles[1], N. Flament[1,2], and D. Müller[1]

[1]School of Geosciences, University of Sydney, Sydney, New South Wales, Australia, [2]Now at School of Earth and Environmental Sciences, University of Wollongong, Wollongong, New South Wales, Australia

Key Points:
- We simulate the role of mantle flow on eastern Australia drainage evolution over the last 150 Ma
- Distinct features of present-day landscape (river longitudinal profiles, Murray-Darling basin shape) are reproduced by the model
- The model predicts the drainage reversal of proto-Murray river driven by the Cretaceous phase of eastern Highland uplift

Correspondence to:
T. Salles,
tristan.salles@sydney.edu.au

Citation:
Salles, T., N. Flament, and D. Müller (2017), Influence of mantle flow on the drainage of eastern Australia since the Jurassic Period, *Geochem. Geophys. Geosyst.*, *18*, 280–305, doi:10.1002/2016GC006617.

Received 2 SEP 2016
Accepted 27 DEC 2016
Accepted article online 3 JAN 2017
Published online 25 JAN 2017

Abstract Recent studies of the past eastern Australian landscape from present-day longitudinal river profiles and from mantle flow models suggest that the interaction of plate motion with mantle convection accounts for the two phases of large-scale uplift of the region since 120 Ma. We coupled the dynamic topography predicted from one of these mantle flow models to a surface process model to study the evolution of the eastern Australian landscape since the Jurassic Period. We varied the rainfall regime, erodibility, sea level variations, dynamic topography magnitude, and elastic thickness across a series of experiments. The approach accounts for erosion and sedimentation and simulates catchment dynamics. Despite the relative simplicity of our model, the results provide insights on the fundamental links between dynamic topography and continental-scale drainage evolution. Based on temporal and spatial changes in longitudinal river profiles as well as erosion and deposition maps, we show that the motion of the Australian plate over the convecting mantle has resulted in significant reorganization of the eastern Australian drainage. The model predicts that the Murray river drained eastward between 150 and ~120 Ma, and switched to westward draining due to the tilting of the Australian plate from ~120 Ma. First order comparisons of eight modeled river profiles and of the catchment shape of modeled Murray-Darling Basin are in agreement with present-day observations. The predicted denudation of the eastern highlands is compatible with thermochronology data and sedimentation rates along the southern Australian margin are consistent with cumulative sediment thickness.

1. Introduction

Over the last 30 years, mantle flow has been shown to affect the evolution of continental-scale topography [e.g., *Hager and Richards*, 1989; *Cazenave et al.*, 1989; *Lithgow-Bertelloni and Gurnis*, 1997; *Gurnis et al.*, 1998; *Müller et al.*, 2008; *Heine et al.*, 2010; *Moucha and Forte*, 2011; *Flament et al.*, 2015; *Müller et al.*, 2016a]. Estimations from these predictive models are often calibrated using present-day and geological constraints on mantle flow induced dynamic topography. These observations mainly rely on sparse data sets from which expressions of dynamic topography are inferred by computing residual depth anomalies with respect to reference models of oceanic or continental topography [see *Flament et al.*, 2013, for a review]. Despite some progress [*Winterbourne et al.*, 2014; *Hoggard et al.*, 2016], extracting reliable estimates of residual topography from these observations is generally difficult and therefore quantitative predictions of dynamic topography remain difficult to calibrate.

On the other hand, long-term landscape dynamics could be used to evaluate and discriminate between past geodynamic processes [e.g., *Conrad and Gurnis*, 2003; *Bishop*, 2007; *Simoes et al.*, 2010] as they record the interactions of deep and surface processes [e.g., *Avouac and Burov*, 1996; *Bonnet and Crave*, 2003; *Whipple and Meade*, 2006]. Geomorphic processes accounting for fluvial incision and hillslope mechanisms are used in regular models of landscape evolution to understand temporal evolution of landscape and sediment fluxes as a response to tectonic and climatic forcings [e.g., *Davy and Crave*, 2000; *Howard et al.*, 1994; *Sklar and Dietrich*, 2006; *Whipple and Tucker*, 1999; *Tucker and Slingerland*, 1997; *Tucker and Bras*, 1998; *Tucker and Hancock*, 2010]. Such models generally focus on temporal scales up to a few hundred thousand years and spatial scales up to a few hundred kilometers (i.e., mesoscale), and many applications focus on understanding orogenic responses to tectonic or climatic forcings [e.g., *Tucker*, 2004; *Whipple and Meade*, 2004, 2006].

Continental-scale landscape dynamics, sediment erosion, and transport in response to long-wavelength dynamic topography occurring over hundreds to thousands of kilometers and tens of million years (i.e.,

macroscale) has only been investigated in few studies [*Braun et al*., 2013; *Ruetenik et al*., 2016]. Over the last decade, several analog models of macroscale topography evolution [*Babault et al*., 2005; *Bonnet and Crave*, 2003; *Lague et al*., 2003] have been designed to better constrain landscape response to different tectonic and precipitation conditions. Numerical studies [*Kooi and Beaumont*, 1996; *Davy and Crave*, 2000; *Simoes et al*., 2010] based on mesoscale laws for fluvial and hillslope processes have indicated that macroscale evolution of landscape is complex and scale-dependent. The scarcity of extensive studies is a consequence of several major limitations. First, refinement of mesoscale landscape evolution models is generally too computationally demanding to be transferred to macroscale. Second, most of these numerical models are based on a mesoscale approximation of channel and hillslope processes. At the scale of these processes paleolandscapes are often unknown and are difficult to appreciate for even larger spatial and temporal scales. Third, paleoclimatic proxy data are sparse and must be extrapolated over extensive areas. Even though these constraints limit the predictive power of any macroscale simulation, such models can provide meaningful insights into the fundamental links between continental-scale dynamic topography, landscape and drainage evolution, fluvial erosion, and deposition.

Here we use the dynamic topography predicted by a paleogeographically constrained reconstruction of past mantle flow [*Bower et al*., 2015; *Müller et al*., 2016a] to evaluate the formation of the Australian Great Dividing Range over the last 150 Myr and quantify the influence of mantle flow on continental-scale morphological features using *Badlands* [*Salles and Hardiman*, 2016]. Using low-resolution models (20 km), we first explore the sensitivity of landscape evolution models rainfall conditions, dynamic topography magnitude, flexural thickness, and sediment erodibility. The success of these exploratory models is evaluated by comparing the simulated cumulative erosion with denudation rate for the Great Dividing Range and the difference between model final elevation and topography taken from ETOPO5 [*National Geophysical Data Center* (*NOAA*), 2006]. A high-resolution model (5 km), based on parameters selected from the sensitivity analysis, is then used to quantify the time dependence of erosion and deposition on smaller scales, as well as the evolution of catchment dynamics, drainage capture, and drainage network reorganization. We show that the motion of the Australian plate over the convecting mantle resulted in significant changes in river drainage, intercontinental erosion, and sedimentation. Despite the assumptions and limitations inherent in this study, predicted cumulative denudation and sedimentation are compatible with thermochronology data in the Australian eastern highlands, with cumulative sediment thickness in a southern Australian offshore basin and with present-day river profiles and catchments.

In the future, the approach we introduce here may be particularly relevant to understand sediment routing and associated basin formation and evolution at continental scale in regions far from plate margins or where lithospheric deformation is not significant. It could also be used to derive some quantitative constraints for the dynamic topography history obtained from global mantle flow models.

2. Methods

2.1. Model Description

2.1.1. Modeling Past Mantle Flow and Dynamic Topography

We reconstruct past mantle flow by driving *CitcomS* [*Zhong et al*., 2008] incompressible convection models with plate velocities as time-dependent boundary conditions and progressively assimilating the thermal structure of the lithosphere and of shallow slabs [*Bower et al*., 2015] derived in 1 million year intervals from a plate reconstruction. This semiempirical modeling is guided by the current intractability of computing time-dependent models of the plate-mantle system with a resolution sufficient to dynamically obtain tectonic-like features, including one-sided subduction [*Stadler et al*., 2010]. The approach allows us to reconstruct past mantle flow for times before 100 Ma, and it ensures the computations follow Earth's imposed tectonic history.

The model consists of $128\times128\times64\times12 \approx 12.6\times10^6$ elements, and radial mesh refinement gives average resolutions $\sim50\times50\times15$ km at the surface, $\sim28\times28\times27$ km at the core-mantle boundary, and $\sim40\times40\times100$ km in the midmantle.

The thickness and temperature of the lithosphere are derived using a half-space cooling model and the synthetic age of the ocean floor for the initial condition and progressive data assimilation [*Bower et al*., 2015]. The global thermal structure of slabs, assimilated in the model to 350 km depth in 1 million year increments, is constructed from the location and polarity of subduction zones and from the age of the ocean floor [*Bower et al*., 2015].

The Rayleigh number that determines the vigor of convection is

$$Ra = \frac{\alpha_0 \rho_0 g_0 \Delta T h_M^3}{\kappa_0 \eta_0}, \quad (1)$$

where $\alpha_0 = 3 \times 10^{-5}$ K^{-1} is the coefficient of thermal expansion, $\rho_0 = 4000$ kg m^{-3} is the density of the mantle, $g_0 = 9.81$ m s^{-2} is the acceleration of the gravity field, $\Delta T = 2825$ K is the temperature change across the mantle, $h_M = 2867$ km is the thickness of Earth's mantle, $\kappa_0 = 1 \times 10^{-6}$ m^2 s^{-1} is the thermal diffusivity, $\eta_0 = 1 \times 10^{21}$ Pa s is the viscosity and the subscript "0" indicates reference values. The above listed values give $Ra = 7.8 \times 10^7$.

The viscosity depends on pressure and temperature as

$$\eta = \eta_0(r) \exp\left(\frac{E_\eta}{R(T+T_\eta)} - \frac{E_\eta}{R(T_b+T_\eta)}\right), \quad (2)$$

where $\eta_0(r)$ is a prefactor defined with respect to the reference viscosity, set equal to 1 for the upper mantle (above 660 km depth) and to 100 for the lower mantle. E_η is the activation energy set to 100 kJ mol^{-1} in the upper mantle and to 30 kJ mol^{-1} in the lower mantle, $R = 8.31$ J mol^{-1} K^{-1} is the universal gas constant, T is the dimensional temperature, $T_\eta = 452$ K is the temperature offset and $T_b = 1685$ K is the background mantle temperature. These activation energy and temperature offset limit variations in viscosity to three orders of magnitude across the range of temperatures.

Air-loaded dynamic topography is obtained by scaling the surface vertical stress σ_{rr} resulting from mantle flow according to

$$h = \frac{\sigma_{rr}}{\Delta\rho\, g_0}, \quad (3)$$

where $\Delta\rho = 3340$ kg m^{-3} is the density difference between the shallow mantle and air. Dynamic topography is derived in a series of instantaneous Stokes-flow calculations based on snapshots of the temperature and velocity fields from the main model run, in which the surface boundary condition is no-slip and the uppermost 250 km of the mantle do not contribute to the flow. Dynamic topography is calculated as a postprocessing step to make it possible to change the surface boundary condition from imposed tectonic velocities to no-slip, and to ignore buoyancy above a given depth. This depth is chosen because the model contains lithospheric keels up to 250 km thick for continents of Archean tectonothermal age [*Artemieva*, 2006; *Flament et al*., 2014], and we consider that dynamic topography originates beneath the thermal boundary layer of mantle convection [e.g., *Flament et al*., 2013], in this case the assimilated lithosphere. As a consequence, dynamic topography originating shallower than 250 km depth, expected to be large in amplitude [e.g., *Flament et al*., 2013], is not captured by the model.

2.1.2. Landscape Evolution

Many landscape evolution models (LEMs) have been developed over the past decades [e.g., *Braun and Sambridge*, 1997; *Coulthard*, 2001; *Crave and Davy*, 2001; *Davy and Lague*, 2009; *Tucker and Hancock*, 2010; *Braun and Willett*, 2013; *Salles and Duclaux*, 2015] and applied to improve our understanding of mesoscale landscape dynamics over spatial dimensions of an individual catchment to an entire orogen and temporal dimensions of thousands to millions of years [e.g., *Braun and Sambridge*, 1997; *Tucker et al*., 2001; *Willgoose*, 2005; *Tucker*, 2009; *Paola et al*., 2009].

We briefly present the constitutive equations of *Badlands*, the landscape evolution model used here (Figure 1). *Badlands* is an open-source and parallel basin and landscape model designed to simulate both erosion and deposition [*Salles*, 2016] and to investigate drainage evolution over continental scale and hundreds of millions of years. Computations at such scales are achieved by considering simpler physics [*Garcia-Castellanos et al*., 2003; *Braun and Willett*, 2013; *Goren et al*., 2014] and an efficient parallelization implementation based on sub-basin partitioning and load-balancing [*Salles and Hardiman*, 2016, and references therein].

2.1.2.1. Constitutive Equations

The continuity of mass is defined by the standard equation:

$$\frac{\partial z}{\partial t} = -\nabla \cdot \mathbf{q_s} + u, \quad (4)$$

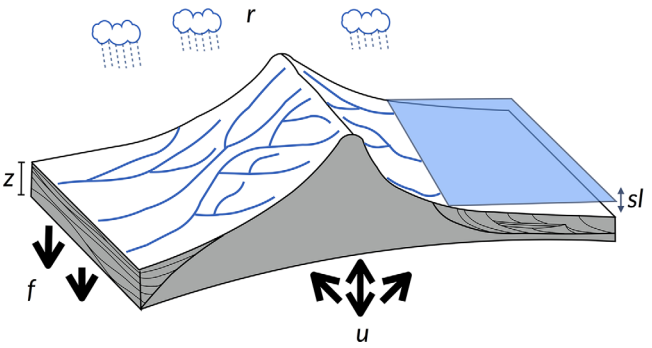

Figure 1. A schematic of 2-D landscape evolution model illustrating the main variables and forces simulated with *Badlands*, where *z* is surface elevation, *r* is rainfall, *sl* is sea level, *f* is flexural isostasy, and *u* is tectonic or dynamic topography.

where u in m yr^{-1} is a source term that represents tectonic or dynamic topography and $\mathbf{q_s}$ is the depth-integrated, bulk volumetric sediment flux per unit width (m^2 yr^{-1}). The sediment transport rate encapsulates both transport by channel flow $\mathbf{q_r}$ and hillslope $\mathbf{q_d}$ [*Chen et al*., 2014, and references therein]. For channel flow, the model is able to simulate both the transport-limited and detachment-limited regimes [*Davy and Lague*, 2009; *Pelletier*, 2011].

In this study, we assume that fluvial erosion and transport is only based on a detachment-limited mode. Therefore, transport by channel flow, $\mathbf{q_r}$, is modeled using the conventional stream power law equation and is defined as a function of topographic gradient ∇z and surface water discharge. Surface water discharge expression relates net precipitation P (which can be uniform or spatially variable) and contributing drainage area A.

$$-\nabla \cdot \mathbf{q_r} = -\epsilon (PA)^m (\nabla z)^n. \tag{5}$$

ϵ, the coefficient of erodibility, is a measure of incision efficiency. The coefficients m and n are both positive and indicate how the incision rate scales with bed shear stress. Their ratio (m/n) is considered to be $\simeq 0.5$, in which case $(PA)^m (\nabla z)^n$ scales with shear stress to a positive power [*Tucker and Hancock*, 2010].

Hillslope processes are defined with a simple creep transport law [*Fernandes and Dietrich*, 1997; *Braun et al*., 2001; *Perron et al*., 2009] of the form:

$$-\nabla \cdot \mathbf{q_d} = -\kappa \nabla^2 z, \tag{6}$$

κ is the diffusion coefficient. The coefficient of erodibility and the diffusion coefficient encompass the influence of climate, lithology, and sediment transport processes [*Howard*, 1980; *Dietrich et al*., 1995; *Whipple and Tucker*, 1999; *Lague et al*., 2005; *Tucker and Hancock*, 2010].

2.1.2.2. Flexural Isostasy

Sediment redistribution by surface processes changes the repartition of surface loads on the elastic outer shell of Earth [*Hodgetts et al*., 1998; *Wickert*, 2015, and references therein]. *Badlands* includes a module that solves lithospheric flexure in two dimensions [*Altas et al*., 1998; *Li et al*., 2004; *Salles and Hardiman*, 2016] using finite differences and that can be used to simulate local or regional isostatic compensation. The equation governing elastic deformation for a uniform flexural rigidity and in the absence of horizontal forces is

$$D\nabla^2\nabla^2\omega + (\rho_m - \rho_f) g\omega = q_l, \tag{7}$$

ω is the vertical deflection of the plate and ρ_m and ρ_f are the densities of the mantle and of the filling material (either sediments, air or water or a combination of both), respectively, $q_l = \rho_l g h_l$ with ρ_l and h_l the density and height of the load. D is the flexural rigidity of an elastic plate

$$D = \frac{ET_e^3}{12(1-\nu^2)}, \tag{8}$$

where E is Young's modulus, ν is Poisson's ratio, and T_e is the effective thickness.

2.1.2.3. Porosity and Compaction

In *Badlands*, a forward compaction algorithm is coupled to sedimentation and approximate compaction and pore pressure changes in the sedimentary column through time [*Tetzlaff and Harbaugh*, 1989; *Bahr et al*., 2001; *Salles et al*., 2011]:

$$\frac{\partial \phi}{\partial \sigma} = -C_\phi (\phi - \phi_{\min}). \tag{9}$$

σ is the lithostatic stress, ϕ is the porosity (pore volume over total rock volume), and C_ϕ is the compaction coefficient. Following *Bahr et al*. [2001] and rewriting equation (9) as a function of depth and integrating gives

$$\phi_z = \frac{e^{-C_\phi g(\rho_s-\rho_w)z}}{e^{-C_\phi g(\rho_s-\rho_w)z}+\beta}, \tag{10}$$

where ρ_s and ρ_w are the sediment and water density, and $\beta=(1-\phi_{\max})/\phi_{\max}$ with $\phi_{\max}$ the surficial sediment porosity value. Changes induced by sediment compaction are used to adjust both underlying basins sedimentary thicknesses as well as surface elevation.

2.2. Model Setup

2.2.1. Initial and Boundary Conditions to Model Mantle Flow

We use Model 1 of *Müller et al*. [2016a], which is based on the topologically evolving plate boundaries [*Gurnis et al*., 2012] from the global reconstruction of *Müller et al*. [2016b]. In this tectonic setting, continuous west-dipping subduction occurs along eastern Gondwana until 100 Ma, followed by a 15 Ma gap in subduction, before the South Loyalty Basin opens as a back-arc basin between 85 and 55 Ma, after which it is consumed by subduction [see *Müller et al*., 2016a, for a detailed description].

In the initial condition at 230 Ma, slabs are inserted down to the shallower depth between 1400 km depth and the depth derived from the initiation age of subduction zones and global slab sinking rates, assuming a descent rate of 3 cm yr^{-1} in the upper mantle and 1.2 cm yr^{-1} in the lower mantle. Similarly, subduction zones that appear during the model run are progressively inserted in the upper mantle based on initiation age and global slab descent rates. Slabs are initially twice as thick in the lower mantle compared to their thickness in the upper mantle, to account for advective thickening in the more viscous lower mantle. Slabs initially dip at 45° down to 425 km depth and dip at 90° below 425 km depth. The initial condition includes a 113 km thick thermochemical layer at the base of the mantle in which material is chemically ~4.2% denser than ambient mantle. This setup suppresses the formation of active mantle plumes and allows us to focus on subduction-driven dynamic topography [*Flament et al*., 2014].

To analyze the sensitivity of the landscape evolution model to the dynamic topography derived from Model 1 of *Müller et al*. [2016a], we scaled its magnitude from 0.5 to 2.0 using 0.5 increments (models 10–13, Table 1). This test captures variations in the amplitude of predicted dynamic topography based on the assumed load (air, water, or sediment), boundary condition (free-slip, no-slip, or plate velocities) and depth above which sources of buoyancy are ignored. The amplitude of dynamic topography is greater for no-slip than for free-slip boundary conditions, increases when shallower sources of buoyancy are considered and increases with the density of the assumed load. Note that we did not apply a time-dependent water-loading or sediment-loading [*Austermann and Mitrovica*, 2015] in areas below sea level and undergoing sedimentation.

2.2.2. Initial and Boundary Conditions to Model Landscape Evolution

2.2.2.1. Past Sea Level

Long-term global sea level fluctuations have long been recognized through their effects on depositional patterns on continental platforms and margins [*Hallam*, 1984; *Watts and Thorne*, 1984; *Haq et al*., 1987; *Miall*, 1992; *Christie-Blick and Driscoll*, 1995; *Haq and Al-Qahtani*, 2005; *Miller et al*., 2005; *Müller et al*., 2008]. Long-term sea level change is thought to primarily reflect changes in the volume of the ocean basins [*Hays and Pitman*, 1973], and is therefore model-dependent. Here two end-member sea level functions are considered. We first assumed that sea level is constant through the duration of the simulation and is fixed to present day (model 1, Table 1). We then we use the past eustatic sea level of *Haq et al*. [1987] plotted in Figure 2c.

2.2.2.2. Precipitation Evolution

On timescales of tens to hundreds of millions of years, global scale climates are controlled by changes in solar luminosity, continent distribution, ocean circulation, and atmosphere composition [*Veevers*, 1994; *Myers et al*., 2011; *Van Der Meer et al*., 2014]. These changes drive temporal evolution of global rainfall regimes. At continental scale, orographic precipitation [*Roe et al*., 2003; *Whipple*, 2009] controls rock weathering and the downstream distribution in fluvial discharge, which in turn drives fluvial erosion and influences drainage network organization and associated morphology in channel slope and relief across landscapes [*Bonnet and Crave*, 2003; *Anders et al*., 2008; *Bonnet*, 2009; *Giachetta et al*., 2012].

Table 1. Set of Low-Resolution Tests (20 km) Used to Analyze the Sensitivity of the Model to a Series of Parameters: Sea Level, Precipitation (GFDL Indicates Latitude-Dependent Precipitation Following *Delworth et al.* [2006]), Erodibility, Flexural Isostasy, Compaction, and Magnitude of Dynamic Topography and Their Associated Rating (⊖ or ⊕) Based on Comparison to Continental Flooding, Denudation, and Present-Day Topography From Left to Right

Model	Sea Level	Rain (m yr^{-1})	Erodibility (yr^{-1})	Flexural Isostasy	Compaction	Dynamic Topography Magnitude	Rating
1	Constant	1	5×10^{-8}	×	×	1.0	⊖⊖⊖
2	*Haq* 87	GFDL	1×10^{-8}	T_e = 24 km	×	1.0	⊕⊖⊖
3	*Haq* 87	GFDL	3×10^{-8}	T_e = 24 km	×	1.0	⊕⊖⊖
4	*Haq* 87	GFDL	5×10^{-8}	T_e = 24 km	×	1.0	⊕⊕⊖
5	*Haq* 87	GFDL	8×10^{-8}	T_e = 24 km	×	1.0	⊕⊕⊕
6	*Haq* 87	GFDL	1×10^{-7}	T_e = 24 km	×	1.0	⊕⊖⊕
7	*Haq* 87	GFDL	5×10^{-8}	T_e = 70 km	✓	1.0	⊕⊕⊖
8	*Haq* 87	GFDL	8×10^{-8}	T_e = 70 km	✓	1.0	⊕⊕⊕
9	*Haq* 87	GFDL	1×10^{-7}	T_e = 70 km	✓	1.0	⊕⊖⊕
10	*Haq* 87	1	5×10^{-8}	×	✓	0.5	⊖⊕⊖
11	*Haq* 87	1	8×10^{-8}	×	✓	1.0	⊕⊕⊕
12	*Haq* 87	1	1×10^{-7}	×	✓	1.5	⊕⊖⊖
13	*Haq* 87	1	2×10^{-7}	×	✓	2.0	⊕⊖⊖

In this study, we define two types of rainfall pattern. The first one consists of a constant precipitation value set to 1 m yr^{-1} and which is uniform both spatially and temporally during the 150 Ma of the simulation (models 1, 10–13, Table 1). The second precipitation conditions are reconstructed based on present-day climate and geological plate tectonic evolution (models 2–9, Table 1). We use an annual precipitation regime assumed to be uniform over a longitudinal extent ranging between 135°E and 155°E and averaged at a given latitude by the GFDL CM2.1 model over the period 1951–2000 [*Delworth et al.*, 2006]

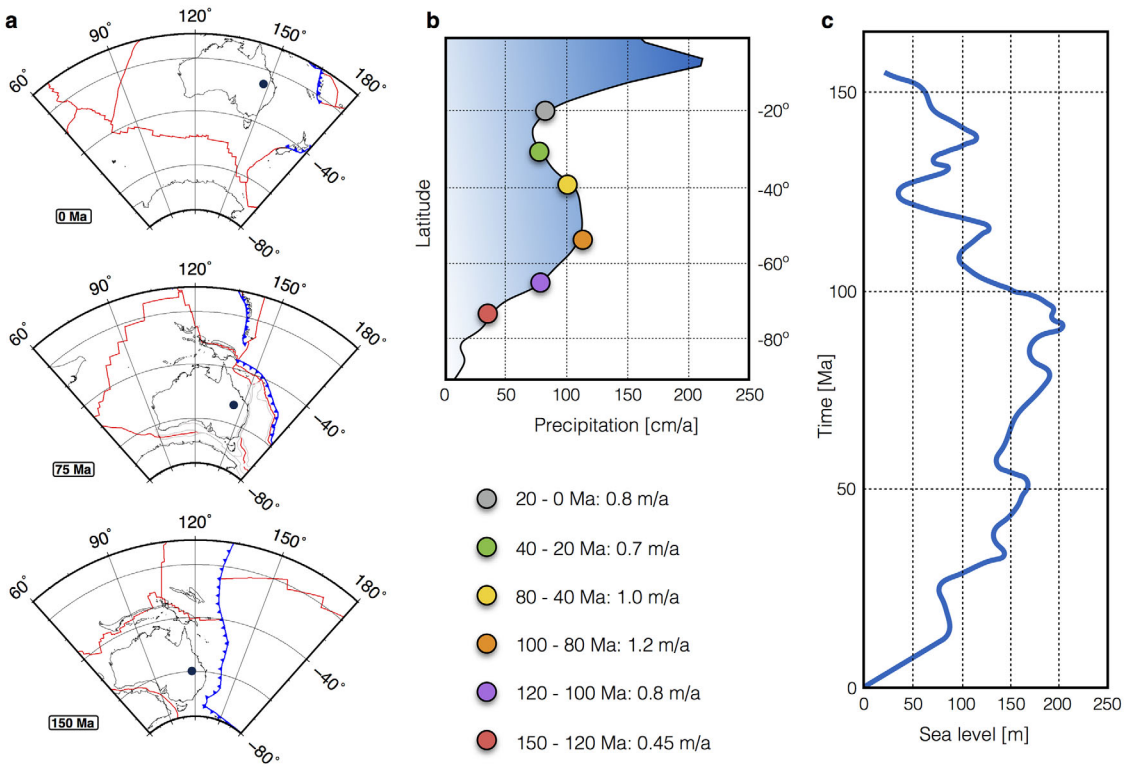

Figure 2. (a and b) Modeling the evolution of Australian precipitation over the last 150 Myr based on the latitudinal position of the continent obtained from the solid Earth model and 50 years longitudinal averaged precipitation modeled by NOAA/GFDL CM2.1 for the southern hemisphere [*Delworth et al.*, 2006]. Past values of precipitation are deduced from the past latitude of the dark circle shown in (a) and the precipitation model shown in (b). In (a), reconstructed coastlines are shown in black, subduction zones in blue with triangles on the over-riding plate, mid-ocean ridges and transform faults in red and deforming areas in gray. (c) Long-term sea level fluctuations relative to present-day [*Haq et al.*, 1987].

(Figure 2b). The latitudinal position of the Australian Plate for the last 150 Ma is derived from the plate tectonic history and used to calculate the spatial rainfall values at any given simulation time steps (Figure 2a). This simple approach interpolates the last 50 years of the latitudinal distribution of precipitation through the model simulation time. In the future, we plan on improving the rainfall spatial and temporal distribution pattern by combining outputs from paleoclimate reconstruction models with an orographic precipitation module.

2.2.2.3. Paleotopography Construction

Our hypothesis is that the present-day topography of Australia was partly shaped by mantle-driven dynamic topography. To obtain the large-scale paleotopography at 150 Ma, we subtract the predicted present-day dynamic topography from the global digital elevation model (DEM) ETOPO5 [*NOAA*, 2006]. A Gaussian filter is then applied to eliminate present-day drainage patterns and flow networks. This surface is further adjusted by removing ocean sediment thickness accumulated over the last 150 Myr based on total sediment thickness maps of the world's oceans and marginal seas [*Whittaker et al*., 2013]. Estimated long-term fluctuations in past eustatic sea level [*Haq et al*., 1987] are then added to the grid to obtain a time-dependent paleo-DEM. Finally, paleoshoreline positions given in the Paleogeographic Atlas of Australia [*Langford et al*., 1995] are used to evaluate and refine the initial paleosurface. The approach consisted in comparing the paleoshoreline locations at different time intervals and by assessing the predicted inundation of the continental areas over the past 150 Ma. The evaluation is further refined based on fossil-derived paleoenvironment interpretation from the aforementioned Paleogeographic Atlas [*Langford et al*., 1995]. The method is similar to the one proposed by *Heine et al*. [2015]. Despite the uncertainties of both local paleoenvironment interpretations and resultant paleoshoreline locations, the initial paleosurface (Figure 6 at 150 Ma) provides a first-order representation of continental-scale topographic elevation for Eastern Australia. From this $\simeq$10 km resolution regular grid, we build a 4000 $\times$ 5500 km triangular irregular surface with an averaged resolution of 5 km. For the sensitivity analysis, the resolution is 20 km.

2.2.2.4. Surface Processes Parameters

The surface evolves according to hillslope and channeling processes in the forward landscape evolution model.

Channel flow erosion is defined through the stream power law equation (equation (5)) with a dimensional erosion coefficient that aggregates several factors including climate and rock type, channel width and hydraulics, among others [*Howard and Kerby*, 1983; *Sklar and Dietrich*, 1998; *Whipple and Tucker*, 1999; *Montgomery*, 2001; *Braun and Willett*, 2013; *Lague et al*., 2005]. This erodibility coefficient ϵ is assumed to be spatially uniform over the entire region and the following range of values are used in our sensitivity analysis tests 1×10^{-8}, 3×10^{-8}, 5×10^{-8}, 8×10^{-8}, and 1×10^{-7} $m^{(1-2m)}$ yr^{-1}. The values for m and n are set to 0.5 and 1. These values are derived for the unit stream power model [e.g., *Whipple and Tucker*, 1999], although other values can be found in the literature [*Gasparini and Brandon*, 2011].

Hillslope processes are implemented through the linear diffusion equation (equation (6)) with two uniform diffusion constants κ_1 and κ_2 which are set to 1×10^{-3} and 5×10^{-3} m^2 yr^{-1}, for aerial and marine environments, respectively [*Pelletier*, 2004; *Sweeney et al*., 2015]. The higher value for constant κ_2 accounts for the reworking of sediments by waves and currents in the marine domain.

2.2.2.5. Flexure and Compaction Related Inputs

The impact of sediment load redistribution by surface processes on the lithosphere is simulated using the flexural isostasy module (equation (7)). For this study, we perform a series of tests with and without flexural isostasy. In cases where the module is turned on, the flexural rigidity of the Australian elastic plate is assumed to be uniform over the entire region and the effective thickness of the plate is set to either 24 or 70 km. The first effective thickness is based on an averaged of the values obtained by *Swain and Kirby* [2006] from wavelet transforms of gravity and topography using the method of *Forsyth and Vetzal* [2002] for the east coast of Australia. The second one is in the upper range of the 45–77 km estimated for eastern Australia by *Zuber et al*. [1989] and *Simons et al*. [2000]. The average sediment and mantle densities are set to 2700 and 3500 kg m^{-3}, respectively.

In some models, we estimate sediment compaction and porosity variation using a simple approach that lacks some details such as deposit variability or diagenesis, but nonetheless captures the essence of the compaction process. It consists of defining an averaged underlying sediment porosity which depends on the overlying load. In models where compaction is simulated, the porosity is assumed to vary from 0.6 on

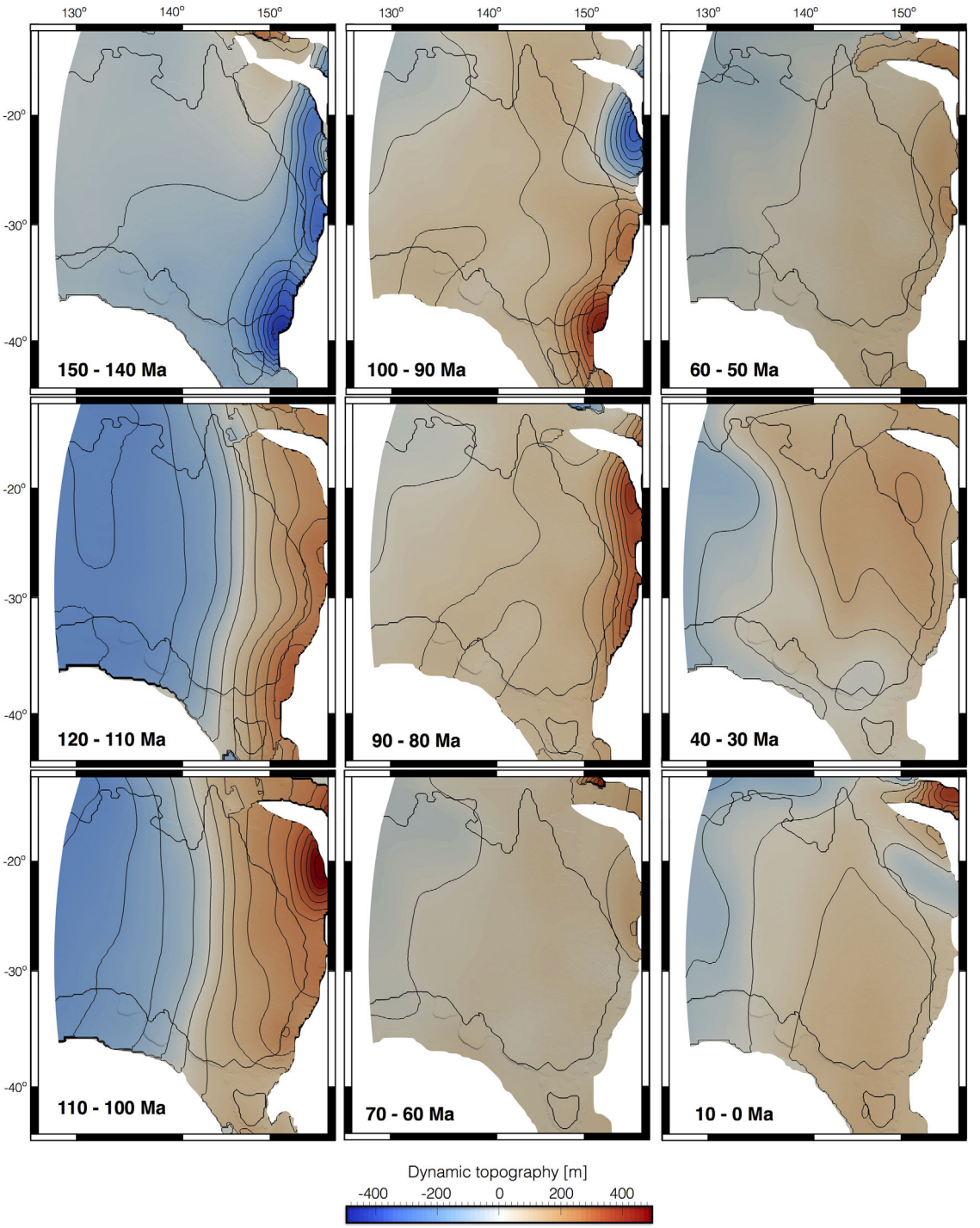

Figure 3. Changes in air-loaded dynamic topography of eastern Australia since 150 Ma, in a fixed Australian reference frame (Model 1 of *Müller et al.* [2016a]) and in 10 Ma increments. Eastern Australia is tilted towards the East Gondwana subduction zone from 150 to 110 Ma. Cessation of subduction and after 100 Ma leads to the dynamic rebound of eastern Australia and a phase of broad uplift and exhumation, continuing from 100 to ~70 Ma. A second phase of stepwise uplift of eastern Australia, starting in the north, and gradually migrating to the south, occurs after ~40 Ma as Australia migrates to the north-northeast, gradually overriding the edge of the large Pacific mantle upwelling. This dynamic topography model is used to drive paleodrainage dynamics in the landscape model.

the surface where the overburden pressure is 0 MPa, to 0.25 for deeply buried sediments. This porosity evolution approximates an exponential function (equation (10)) trend that is supported by porosity data from compacted shales, silts, and sandstones. The compacted coefficient C_ϕ is set to 3.68×10^{-8} Pa^{-1} [*Bahr et al.*, 2001].

3. Sensitivity Analysis

3.1. Mantle Flow Model Sensitivity

We use the dynamic topography predicted by Model 1 of *Müller et al*. [2016a] since this model best reproduces the uplift history inferred from the inversion of eastern Australian river profiles [*Czarnota et al*., 2014] out of four models presented by *Müller et al*. [2016a] in which plate reconstruction and mantle viscosity were varied.

3.2. Landscape Evolution Model Sensitivity

A set of 13 models with resolution 20 km was ran to evaluate the sensitivity of Australian landscape evolution to the forcing parameters described in section 2.2 and summarized in Table 1. Each model is rated based on three criteria. We first evaluate the formation and retreat of the epicontinental sea (left circle in the rating column of Table 1). We then compare the simulated cumulative erosion with estimated denudation rates for the Great Dividing Range (central circle). Lastly, we map the difference in elevation between the simulated final topography and the digital elevation model ETOPO5 [2006] (right circle in Table 1).

3.2.1. Timing of Epicontinental Sea Formation and Retreat

With the exception of model 1 (left plots of Figure 4), all models predict flooding of central Australia between 125 and 80 Ma. The formation of this epicontinental sea is supported by geological observations which document widespread Cretaceous flooding of eastern Australia [*Gallagher and Lambeck*, 1989] and is linked to the combination of sea level rise with the tilting of eastern Australia down to the east due to active subduction. In models 10–13, the extent and timing of the flooding is controlled by the magnitude of the dynamic topography with the flooding starting sooner 125 Ma for model 13 and lasting for more than 45 Ma in contrast to model 10 where it starts at 95 Ma and last for 10 Ma. The maximum flooding occurs between 110 and 100 Ma for all models except models 1 and 10, which is in agreement with estimations from geological observations [*Veevers*, 1984]. The marine inundation of Australia and the eustatic sea level curve of *Haq et al*. [1987] are out of phase with Australia becoming progressively exposed, with disappearance of the epicontinental sea before 80 Ma, when eustatic sea level is close to its maximum (Figure 2c) [*Gurnis et al*., 1998]. From this analysis, models with constant sea level (model 1) and with halved dynamic topography amplitude (model 10) were given a negative score.

3.2.2. Comparisons With Observed Denudation Rates

Here we focus on the impact of the coefficient of erodibility used in the stream power law model (models 2–6 in Table 1) on the erosion of the eastern Australian landscape (Figure 5, bottom maps). Comparisons are carried out on the cumulative erosional changes rather than denudation rate evolution over time which is discussed in details for the high-resolution model. From models 2 to 6, the maximum erosion rate is located along the southeastern part of the Great Dividing Range which is in agreement with other studies realized in the region [*O'Sullivan et al*., 2000]. The erosion rate varies significantly between models, with values ranging from 7 m Myr^{-1} for the lowest erodibility coefficient (1×10^{-8} yr^{-1}) to 22 m Myr^{-1} for the highest one (1×10^{-7} yr^{-1}). Mean averaged denudation rates derived from apatite fission track thermochronology are estimated to be around 15 m Myr^{-1} during the last 150 Ma for southeastern Australia [*Kohn et al*., 2002, 2005], which is consistent with values obtained using erodibility coefficient of 5×10^{-8} and 8×10^{-8} yr^{-1}. Similar results are obtained for models 7–9 where the elastic thickness has been increased to 70 km. These three models show lower denudation rates than the ones with smaller elastic thickness for an equivalent erodibility coefficient. As an example model 9 has an averaged denudation rate of 20.5 m Myr^{-1}, 1.5 m Myr^{-1} smaller than model 6. Using denudation rate between 12.5 and 17.5 m Myr^{-1} as an acceptable range, models 2, 3, 6, 9, 12, and 13 were given a negative score.

3.2.3. Evaluation of Simulated Present-Day topography

The Great Divide comprises a series of low mountain ranges and plateaus roughly paralleling the eastern coasts of Australia for approximately 3700 km [*Oilier*, 1982]. The range begins in the north on Cape York Peninsula (Queensland) where its average elevation varies between 600 and 900 m with maximum topography as high as 1500 m in the Bellenden Ker and McPherson ranges and the Lamington Plateau [*Jennings and Mabbutt*, 1986]. Further south the Australian Alps, near the New South Wales-Victoria border, contain Australia's highest peak, Mount Kosciuszko, with an elevation of 2228 m. The highlands finally bend westward in Victoria to terminate in the Grampians [*Oilier*, 1982], while a southern spur emerges from the Bass Strait to form the central uplands of insular Tasmania. For models with dynamic topography magnitude larger than 1.0 (models 12 and 13) or erodibility coefficient lower or equal than 5×10^{-8} yr^{-1} (models 1, 2, 3, 4, and 7), the simulated present-day

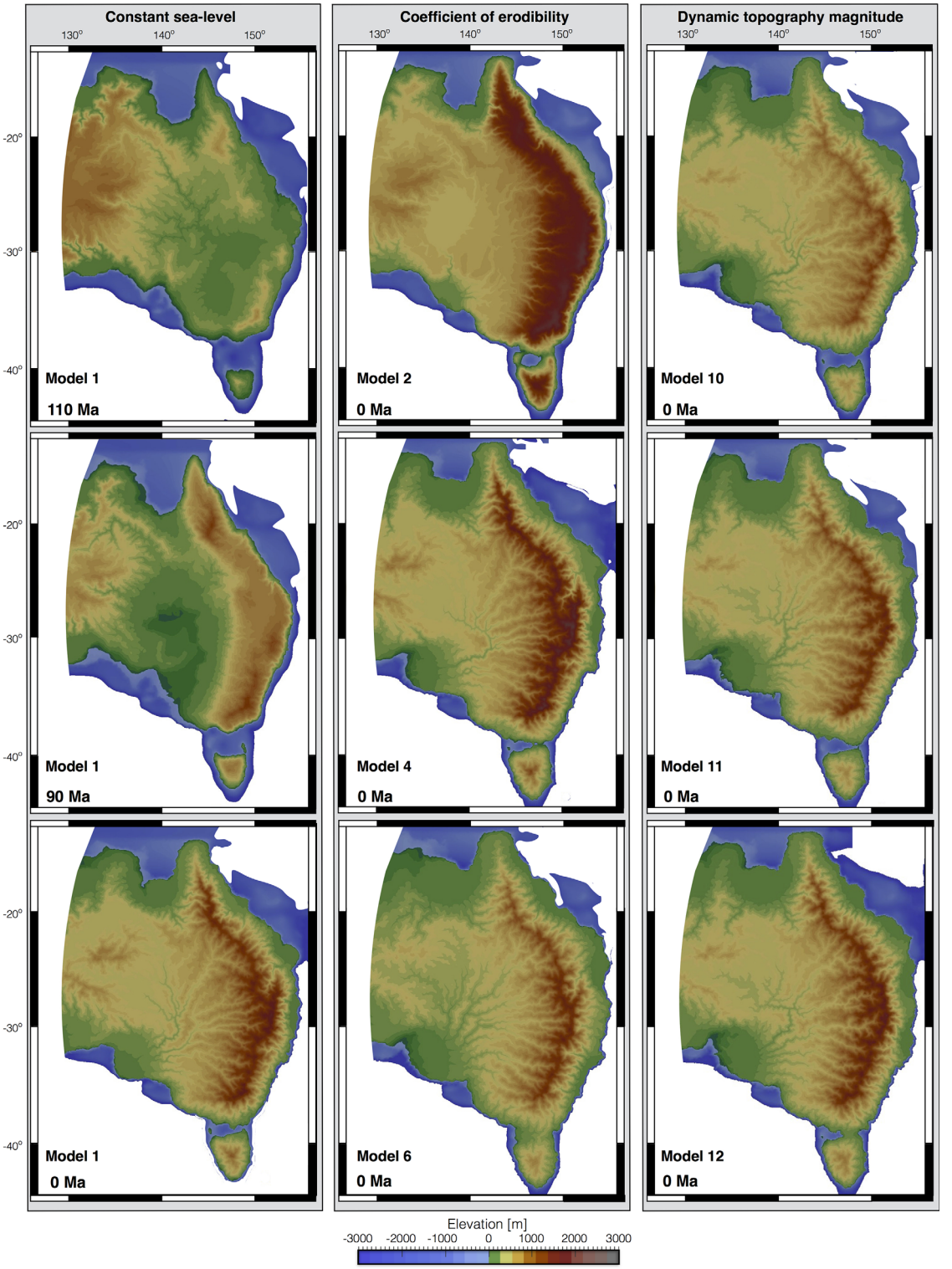

Figure 4. Results of predicted evolution of eastern Australian topography at ≃20 km resolution for some of the models used in the parameter sensitivity tests (as described in Table 1). The maps are colored by elevation relative to sea level. Left panels show the evolution at 110, 90, and 0 Ma for model 1 where sea level is assumed constant, flexural isostasy, and compaction are not computed and rainfall is uniform through space and time. Central panels show the final landscape morphology induced by different coefficients of erodibility using similar sea level, precipitation and flexural conditions. The impact of changing the dynamic topography magnitude derived from the preferred Model 1 of *Müller et al*. [2016a] on final landscape morphology is presented in the right plots.

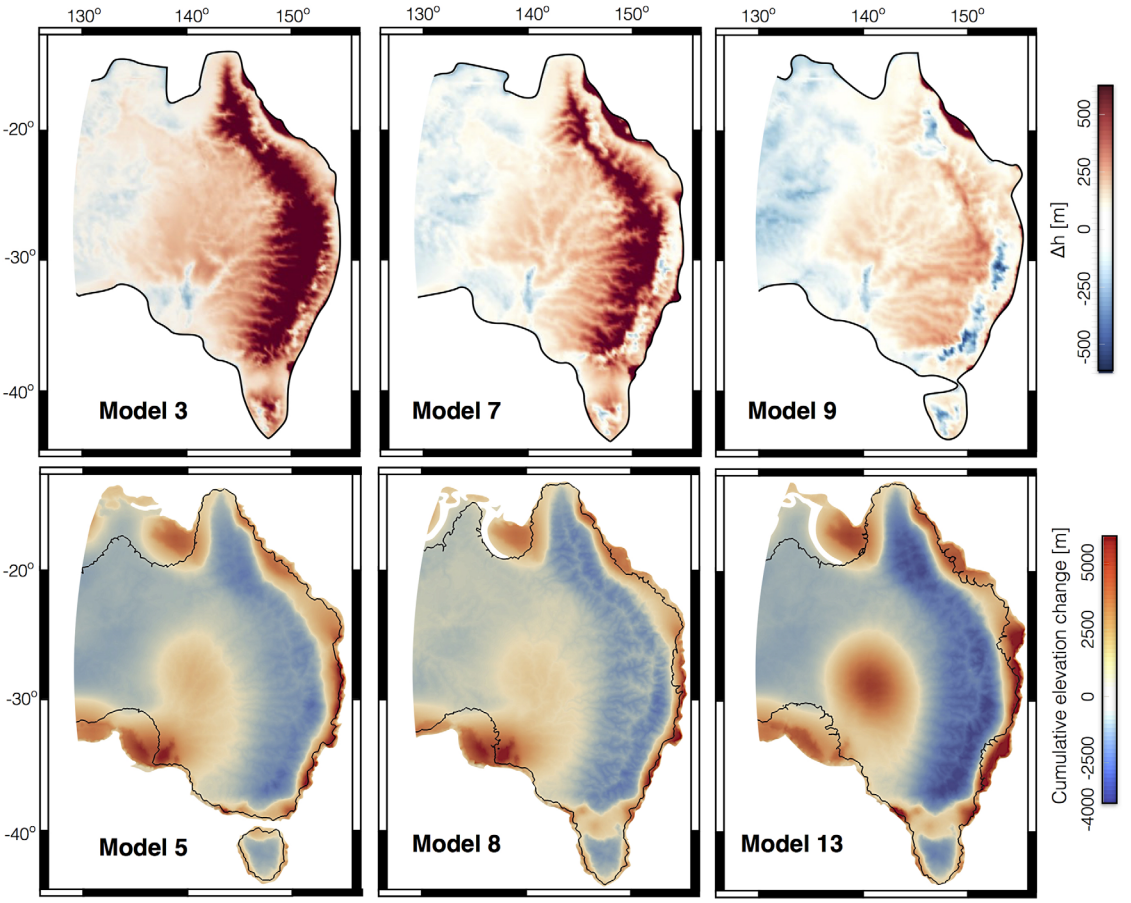

Figure 5. The difference Δh between predicted final topography and ETOPO5 [*NOAA*, 2006] for models 3, 7, and 9 (Table 1) is presented on the top plots. The bottom three plots show cumulative erosion and deposition maps over the 150 Myr of the simulation for models 5, 8, and 10.

topography is overestimated with an average elevation for the entire range above 1750 m (Figure 4 and top plots of 5). The only exception is model 10 in which half of the dynamic topography is used and where the model underestimates the Australian Alps topography with a predicted maximum elevation of 1600 m. All other models (5, 6, 8, 9, 11) predict higher elevations ($\Delta h \leq 250$ m) than the observed ones in the southern part of Queensland with an averaged elevation above 1000 m, and on the western side of the Great Divide ($\Delta h \leq 100$ m; see model 9 in Figure 5). Along the Australian Alps, simulated maximum elevation is in agreement with observed elevation with values ranging from $\simeq$2050 m (model 11) to $\simeq$2300 m (model 5). From this analysis, models with erodibility of at least 8×10^{-8} yr^{-1} and with a dynamic topography magnitude scaling of 1.0 were given a positive score (last circle in the rating column from Table 1).

4. High-Resolution Model

Based on the parameter sensitivity analysis and rating criteria presented in the previous section, model 5 was selected as our preferred low-resolution model. We then created a high-resolution model (5 km) with similar initial conditions: the sea level curve from *Haq et al.* [1987], the precipitation evolution obtained from GFDL CM2.1 model [*Delworth et al.*, 2006], an erodibility coefficient equal to 8×10^{-8} yr^{-1}, an elastic thickness equal to 24 km, the dynamic topography magnitude scaling set to 1.0 and with sediment compaction module turned on.

4.1. Eastern Australian *P*aleotopography

Here we simulate the evolution of Eastern Australia topography since Late Jurassic Period (Figure 6) resulting from the combination of forcing conditions described above.

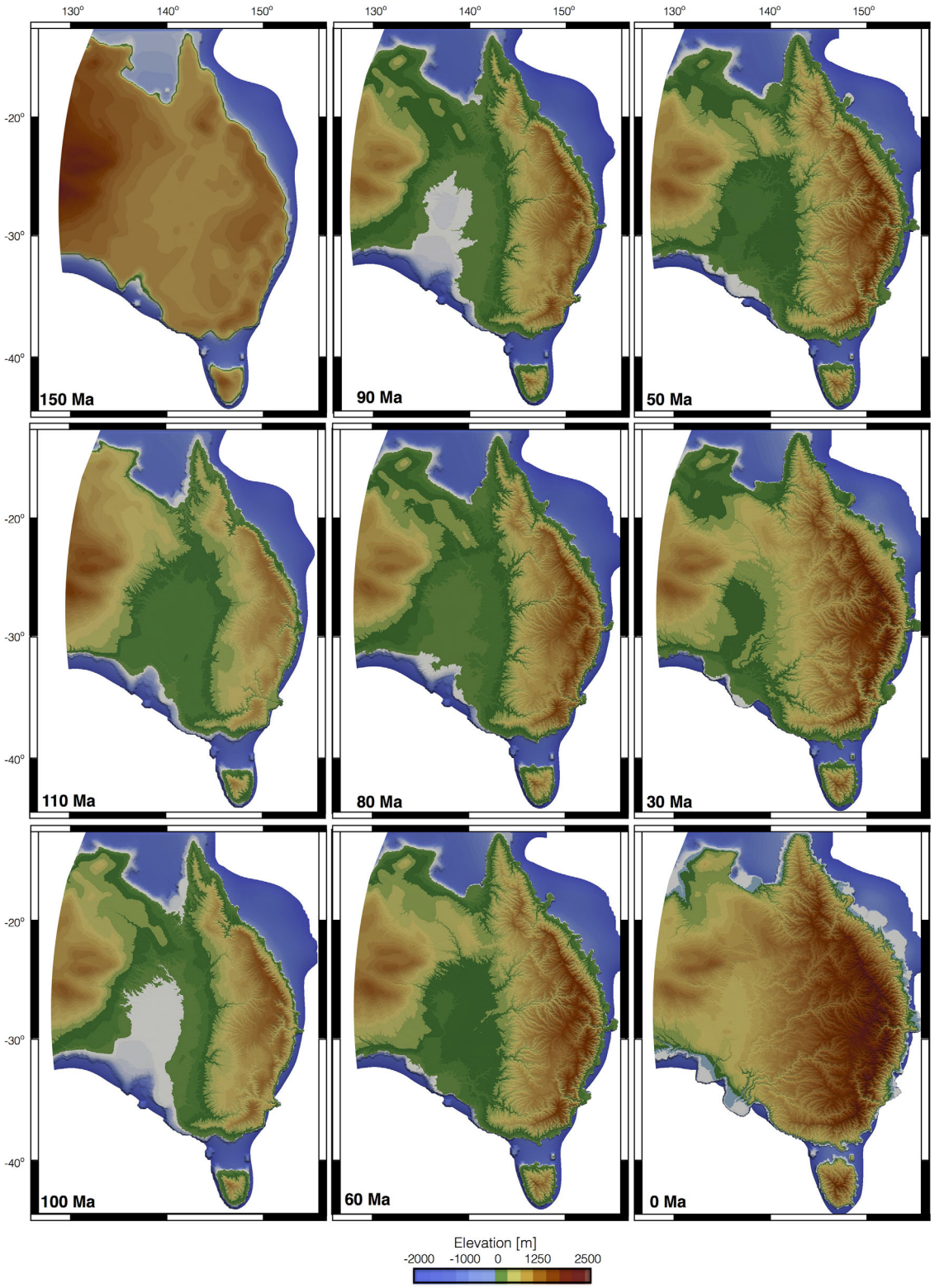

Figure 6. Predicted evolution of eastern Australian topography at ≃5 km resolution. The maps are colored by elevation relative to sea level *Haq et al.* [1987]. The topography at 150 Ma corresponds to the initial model surface derived from the paleotopography reconstruction approach presented in section 2.2.2. The surface evolution is forced using the dynamic topography presented in Figure 3 and the rainfall evolution described in Figure 2. Sediment erosion, transport, and deposition are computed from both hillslope and river processes, and sediment loads are corrected for flexural isostasy and compaction.

The tilting of eastern Australia down to the East Gondwana subduction zone induces an overall subsidence of the region between 150 and ~110 Ma. Because of this tilting, drainage patterns tend to develop primarily following a west to east direction with some major river systems taking their source in the Central Ranges and draining sediment down to the southeastern part of the continent. Large deltaic systems prograde in the marine environment at river mouths. Small fluvial valleys develop following pre-existing or mantle-induced topographic gradients.

The tilting of eastern Australia is reversed to down to the west from ~100 Ma due to the cessation of subduction and eastward motion of the plate over subducting slabs. In conjunction with sea level rise between 110 and 80 Ma, it leads to flooding in central Australia and to a regional reorganization of drainage networks. By 90 Ma, several large deltas are formed in this epicontinental sea with deposition of shallow marine and marginal marine or lacustrine sediments primarily transported from the eastern region. Eastern valleys which were already in place in the early stages of the simulation remain active during this period, with increasing erosion due to base-level change and associated valley incision. By that time, a mean drainage divide emerges that splits the eastern side of Australia into two parts from south to north (Figure 6—90 Ma). The establishment of this drainage divide that only migrates locally over the following 80 Ma marks the early stages of formation of the Great Dividing Range. To the west of the drainage divide, large river systems quickly develop (Figure 6—90 Ma) and several valleys are incised and propagate along the dynamically uplifted region. Local relief increases as valley incision progresses, and the erosion of tributaries increases. The drainage network develops upslope over time (Figure 6—80 Ma) and the highlands are increasingly dissected by the erosion of tributaries. Sediment drained from east to west by these fluvial systems is deposited in a shallow epicontinental sea before its retreat begins at ~85 Ma.

From 80 to 50 Ma, the deposits left behind by the interior sea are now eroded and western flowing river systems from the eastern highlands transport large amounts of sediments toward the southern region, creating vast deltaic provinces. Early stage streams have intensively dissected the highlands that are now drained by a well developed network. Drainage divides are narrowing and overall the landscape is marked by steep slopes down to stream channels.

A second phase of eastern highlands uplift since ~50 Ma is attributed to the north-northeast migration of Australia over the edge of the large Pacific mantle upwelling *Müller et al*. [2016a]. River catchment, drainage organization, and main accumulation regions are stable over this period. On the eastern highlands, this second uplift maintains river gradients steep enough to keep eroding the landscape, further narrowing the drainage divides (Figure 6—30 Ma). In the previously flooded region, the slope is gradually flattening, and the erosive power of rivers is decreasing significantly. Southern deltaic systems are growing and gradually prograding in the marine environment. Over the last 20 Myr, the uplift phase induces the formation of large deltaic/marine deposition areas on the northeast part of the region, which are mainly fed by the eastward-draining river systems of the northernmost eastern highlands (Figure 6—0 Ma). The final topography appears more elevated than observed, which is due to the combined effect of imposed sea level fall (~150 m since ~30 Ma) and dynamic uplift (~100–300 m since ~30 Ma).

4.2. Present-Day Longitudinal River Profiles

Before analyzing the time evolution of drainage patterns, we evaluate the model results by comparing predicted present-day longitudinal river profiles to observed ones (Figure 7), selecting the eight main model rivers closest to eastern Australian rivers considered by *Czarnota et al*. [2014]. These rivers all drain to the coastline and they have been selected to ensure a good representation of the north to south evolution of Australian Great Dividing Range drainage characteristics. All longitudinal profiles exceed Strahler stream order 4, which defines stream size based on a hierarchy of tributaries. The methodology used to extract observed river profile is described in *Czarnota et al*. [2014, and references therein].

Comparisons of observed and simulated longitudinal profiles are presented in Figure 8. The Darling River (Figures 8a and 8a′) exhibits a smooth concave upward profile geometry in the model and in the observations, and profile length (≃2800 km) and elevation (>1000 m) are in agreement between observation and simulation. Several of the simulated rivers draining from the eastern highlands towards the south present a similar trend, suggesting that these rivers have adjusted and minimized downstream stream power despite eustatic, climatic, and tectonic variations.

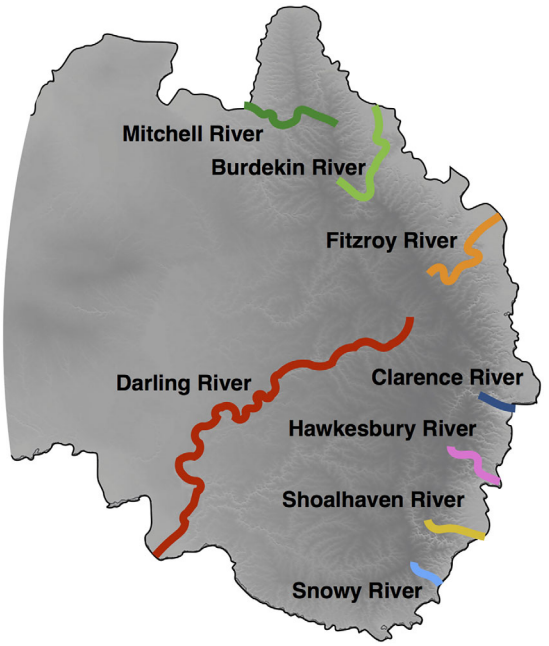

Figure 7. Predicted present-day spatial distribution of main rivers. The eight colored rivers, named using the closest natural rivers occurring in a SRTM data set [*Farr et al*., 2007], are compared to observed rivers in Figure 8.

The following three modeled longitudinal profiles (Mitchell, Burdekin, and Fitzroy rivers plotted in Figures 8b–8d, respectively) have similar length (∼1000 km) and elevation (∼1000 m). Compared to the Darling River, the shape of these river profiles presents steeper gradients and several sharp changes in channel slopes. For the Burdekin River, both the modeled and simulated profiles record a knickzone across tens of kilometers in the first 500 km of the section (Figure 8c). In the model, the formation and upstream migration of this knickzone is related to second phase of uplift of eastern Australia, induced by the large Pacific mantle upwelling since 40 Ma. This knickzone is approximately at the same elevation (>200 m) in the simulated and observed river profiles (Figures 8c and 8c′). However, simulated elevations for these three rivers overestimate observed ones (Figures 8c′ and 8d′), particularly in the case of the Fitzroy River for which the elevation difference is up to 500 m close to the drainage divide. This difference might indicate (1) an overestimation of uplift in the northern part of the eastern highlands during the second phase of uplift since 50 Ma, (2) a regional change in lithology, or (3) climatic conditions which are not taken into account in our simulation.

Most of the southeast facing rivers have irregular, convex-upward shapes (Figures 8e–8h). Knickzones separate segments with lower relief on profiles f to h. These knickzones have similar amplitudes and occur at two common elevations (∼200 and ∼800 m) for the Hawkesbury, Shoalhaven, and Snowy rivers (Figures 8f–8h). These prominent knickzones indicate erosion of the southern part of the Great Escarpment. The spatial correlation across rivers indicates that the pattern of model knickzones is mainly an expression of the dynamic uplift along the south-eastern coast.

Comparisons between simulation and observation show that the model tends to overestimate river lengths. Except for the Fitzroy (Figure 8d) and Hawkesbury (Figure 8f) river profiles, the general trends of elevations are well reproduced by the model. Most simulated profiles exhibit shapes and knickzone patterns similar to the observed ones. Knickzone amplitudes and elevations are consistent between the simulated profiles and can be broadly correlated to the observed ones (particularly for the Burdekin, Figure 8c, and Snowy Rivers, Figure 8h). Despite simplifying assumptions about initial conditions and relatively simple physics, the simulation of eastern Australian landscape evolution reproduces the first-order shape and characteristics of present-day longitudinal river profiles.

4.3. Evolution of Erosion and Deposition

Our model records cumulative erosion and deposition through time and can be used to quantify the implications for landscape evolution and drainage reorganization on deposition of large sedimentary provinces. Here we present the simulated evolution of erosion and deposition during the second phase of the simulation after the retreat of the shallow epicontinental sea 85 Ma ago in the southern part of the area (Figure 9).

From 85 to 60 Ma, drainage patterns gradually develop over the previously flooded, nearly flat area. The first phase of uplift related to the dynamic rebound induced by subduction cessation [*Gurnis et al*., 1998; *Müller et al*., 2016a] results in a broadening exhumation of the eastern Australia highlands from where rivers drain sediments toward the south (Figure 9—75 Ma). Accumulation of sediment is visible along most shorelines and large deltaic provinces develop in the southern region (Ceduna sub-basin). The model predicts most of

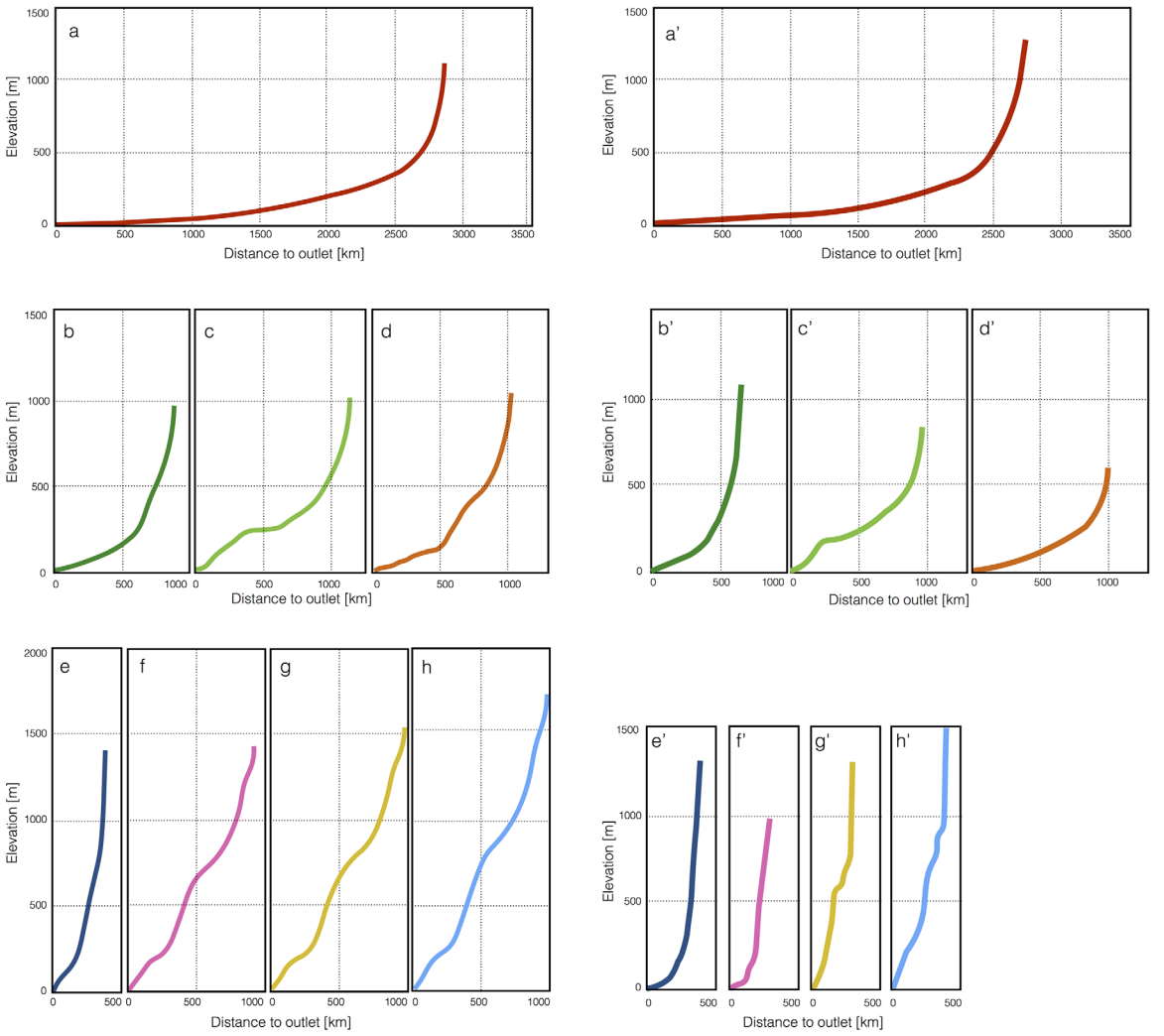

Figure 8. Comparison between simulated (left—a–h) and observed (right—a′–h′) present-day longitudinal river profiles. River profiles are colored following Figure 7. The observed river profiles are selected from *Czarnota et al.* [2014] and are based on a SRTM data set [*Farr et al.*, 2007].

the sediment transported to the southern margin to have been transported by small tributaries located on the southeastern side of the Great Dividing Range and by fully developed drainage systems of the northern Great Dividing Range that have limited erosive power (due to the small topographic gradients in their longitudinal profiles, Figure 9—60 Ma).

Sediment input into the Ceduna sub-basin accelerated substantially between 85 and 50 Ma, which coincides with the second phase of uplift of southeastern Australia (Figure 3), related to its motion over the western rim of the large Pacific mantle upwelling [*Müller et al.*, 2016a]. By 30 Ma, the drainage network on the Great Dividing Range is well developed with large catchments and deep valleys cutting through the eastern highlands (Figure 9—30 Ma). Continuous uplift of the region provides most of the source of sediment accumulating in the Ceduna sub-basin at that time. The erosional engine of sediment routing systems in the eastern areas is mainly dominated by channel flows, with deeply entrenched valleys reflecting the tectonic activity of the region. By the end of the Eocene, the Ceduna sub-basin has accumulated more than 3.5 km of sediment in some areas. Drainage systems are now directly connected to the sub-basin with valleys developed along the entire river paths. Most sediments are transported in large drainage systems characterized by rivers of several thousand kilometers long. Over the last 30 Myr, sediment supplied from the eastern highlands region decreases (Figure 9—20 to 0 Ma) and the model suggests that little accumulation from detrital influx in the Ceduna sub-basin is recorded in the region during this period.

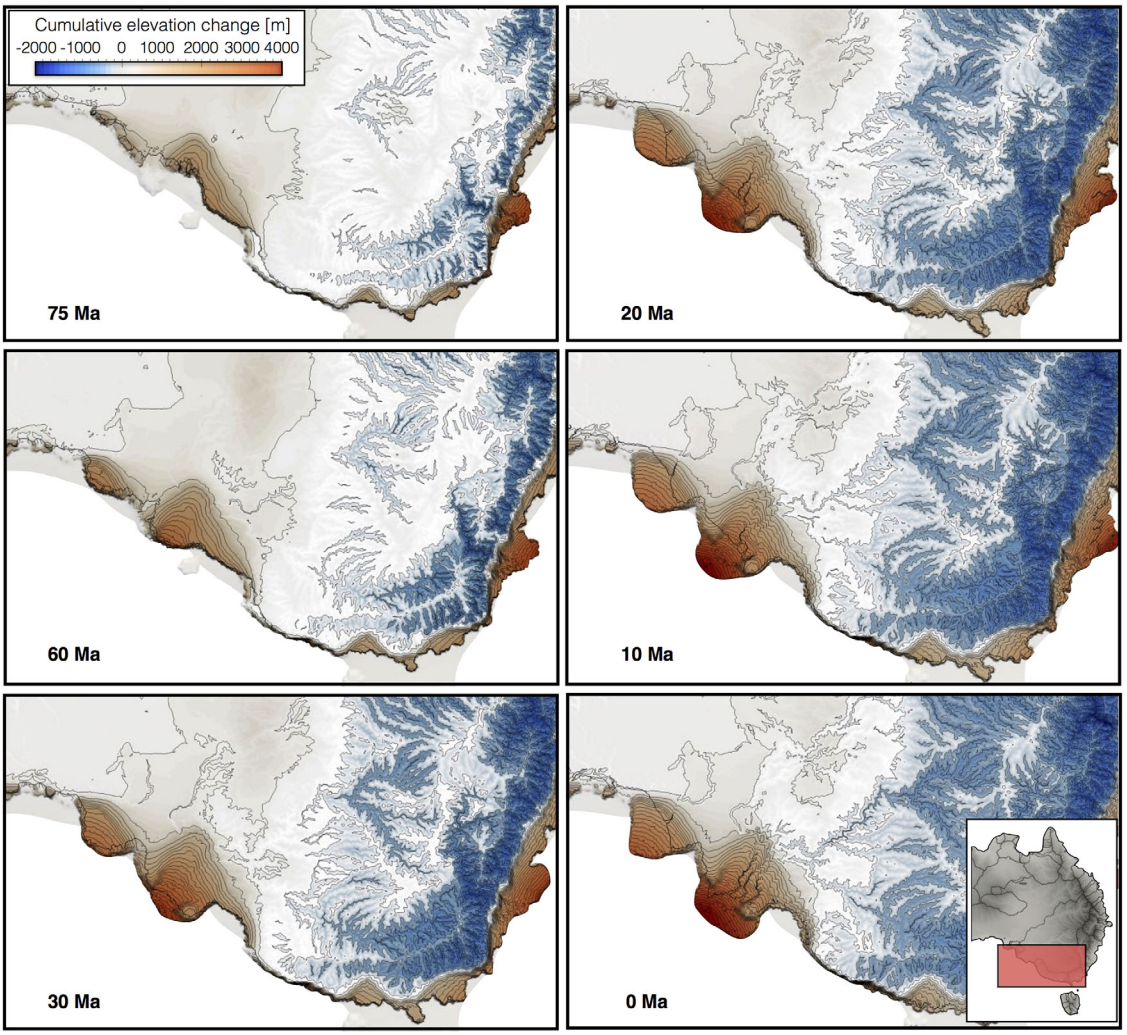

Figure 9. Erosion and deposition maps of the southern part of eastern Australia over the last 75 Myr. Note the progressive erosion of the Great Dividing Range through time and the progradation of deltaic systems in the Ceduna sub-basin.

The distinct two-phase uplift history of the eastern highlands [*Czarnota et al*., 2014; *Müller et al*., 2016a] results in a thick accumulation of sediments in the Ceduna sub-basin. Mantle-induced long-term uplift played a major role in both the construction of the drainage systems of eastern Australia and the Great Dividing Range and in the formation of large deltaic provinces on the southern continental shelf. The model suggests that large river systems (>2000 km in length) were responsible for Cretaceous to Early Eocene accumulation of detrital sediment in the Ceduna sub-basin. This result is consistent with the observations of *Norvick et al*. [2008] and *Lloyd et al*. [2015] who showed that the sediments accumulated in this region during the Cretaceous period seem to be transported from a network of transcontinental rivers.

5. Discussion

5.1. Predicted Denudation History

The model predicts discrete episodes of enhanced denudation would have occurred principally in response to changes in drainage, base-level changes, and uplift. In this study, the denudation only incorporates the mechanical processes of erosion and mass wasting, without accounting for biological and chemical processes [*Smithson et al*., 2008]. Maps of predicted cumulative dynamic topography, erosion, and flexural isostasy (Figures 10a–10c) and temporal profiles for five different locations along the Australian Great Dividing Range (Figures 10d–10g) are used to evaluate the role of dynamic topography and drainage evolution on denudation history.

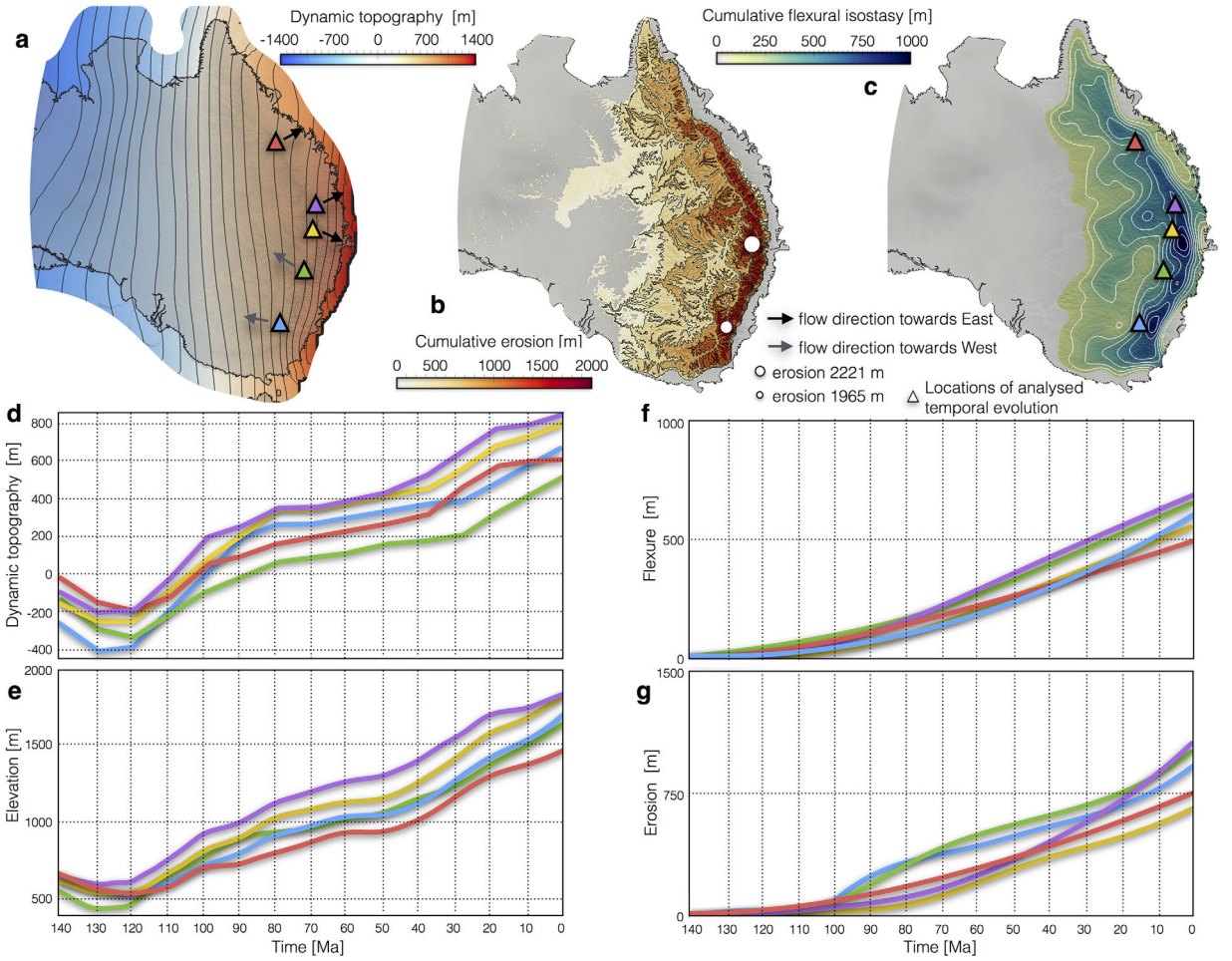

Figure 10. Maps of cumulative model (a) dynamic topography, simulated, (b) erosion, and (c) flexural isostasy, and temporal evolution of (d) cumulative dynamic topography, (e) elevation, (f) flexure, and (g) erosion along the Australian Great Dividing Range for the five locations (triangles) shown in Figure 10c.

Erosion patterns on both sides of the drainage divide show a clear asymmetry between east and west with approximately 3 times more erosion on eastward draining catchments (Figures 10b and 10e). Maximum erosion reaches more than 2 km in the southern region of the range and decreases to an average of 1.4 km on the northern part. The west side present much lower values (∼600 m on average) with higher erosion taking place in few local catchments (up to 1.3 km), which are linked to drainage capture through catchments reorganization. Our flexural isostasy map exhibits a similar trend with induced flexural uplift taking place on a higher rate and on a more restricted regional extent for the eastward flowing catchments in comparison to the westward flowing ones (Figure 10c). The maximum induced flexural uplift is close to 1 km in the southeastern part of the range and decreases toward the north. The assumptions on precipitation, paleogeography, rock erodibility and of only considering the tectonic evolution induced by dynamic topography from mantle convection below 250 km depth clearly limit the predicted denudation magnitude, rates and timing in the region. Nevertheless the results appear to be in first-order agreement with several observations from exhumation estimates in the Snowy Mountains [*O'Sullivan et al.*, 2000], the Sydney Basin [*Faiz et al.*, 2007], the eastern highlands in New South Wales [*O'Sullivan et al.*, 1995] and the Cooper-Eromanga Basin [*Mavromatidis*, 2006] as shown in *Müller et al.* [2016a]. These results demonstrate that the time-dependent interactions between the two phases uplift history derived from the plate-mantle convection model combined with the predictions from the landscape evolution model explain most of the observed spatial denudation history in the region [*Czarnota et al.*, 2014; *Müller et al.*, 2016a].

The temporal profiles for the five selected locations show that the elevation trend is well aligned with the imposed dynamic topography history both in terms of magnitude, rate, and timing (Figures 10d and 10e).

The flexural profiles show a similar trend for all locations with a continuous evolution since 150 Ma and cumulative values ranging between 500 and 600 m (Figure 10f). However the erosion history (Figure 10g) is different between 100 and 70 Ma with higher erosion rates (~25 m/Ma) for the two southernmost profiles. Higher gradients in this region follow the first uplift phase which started at 120 Ma (Figure 10d). The contrast between the five profiles is not related to a difference in tectonic history as they have a similar trend as shown in Figure 10d. Instead, the contrast seems to arise from the rivers' flow directions and related catchment evolution. Between 100 and 90 Ma, the western region is flooded (Figure 6) and the catchments on the southwestern side of the highlands are under active reorganization with increased river incision and length as the epicontinental sea retreats (around 85 Ma). The three other profiles do not show this erosional adjustment as the eastern side is disconnected from the epicontinental sea, river longitudinal profiles are steeper in this region (Figure 11b—90 Ma orange profiles) and catchments much smaller. This result illustrates the primary role of landscape dynamics and particularly of drainage organization on the regional long-term denudation evolution of the region. After a phase of pseudo-stability (between 60 and 30 Ma, with an average denudation rate of ~10 m/Ma), a second episode of accelerated denudation ($\geq$18 m/Ma) is observed on all five profiles. These denudation magnitudes are broadly consistent with the ones obtained in other studies based on apatite fission track thermochronology [*Kohn et al*., 2002, 2005]. In addition, the timings of the two accelerated denudation phases fit the denudation history of southeastern Australia [*O'Sullivan et al*., 2000; *Müller et al*., 2016a].

5.2. Evolution of the Southeastern Australian Landscape

The predicted river profiles (Figure 8) and overall Australian Great Dividing Range elevations (Figure 6) are in agreement with observations. Here we focus on the southeastern part of the region over the last 130 Myr, where the influence of dynamic topography and eustatic sea level variations on catchments reorganization is clearly illustrated (Figure 11). In addition to river longitudinal profiles, we evaluate the stability of the drainage using the χ parameter following similar analyses [*Perron and Royden*, 2012; *Royden and Perron*, 2013; *Yang et al*., 2015]. Analyze of χ profiles shape and temporal evolution is used here to infer the stability of the simulated landscape across southeastern Australia main drainage divide at 90, 60, and 10 Ma (Figure 11b).

At the early stage of river network development, the distribution of flow accumulation (Figure 12) shows that a large catchment area has formed in the southern region with main drainage systems including the proto-Murray River flowing eastward from the Central Ranges. The formation of this drainage system in the southern part of Eastern Australia seems related to the more pronounced tilt reversal existing in the south during that time (Figure 3). From 110 to 90 Ma, the southern region experiences a drainage reversal largely controlled by the dynamic rebound of eastern Australia related to subduction cessation. As a result, the proto-Murray River reverses direction from eastward to westward draining between ~120 and 100 Ma (Figure 12). By 110 Ma, multiple southern catchments have formed on either side of the Great Dividing Range drainage divide.

Before the retreat of the epicontinental sea, multiple catchments have formed on the westward side of the main divide (Figure 11a). Rivers are steep when $\chi \leq 4$ and much more gradual when $\chi \geq 4$ (Figure 11b—90 Ma). Higher χ reflects the low relief of the highlands at that time. The asymmetry between the western and eastern sides of the divide is already well established at this early stage of the range formation, with eastward and southward flowing rivers presenting much steeper gradients and smaller lengths than westward flowing ones (Figure 11b—90 Ma). A large knickzone at ~500 m elevation is visible on two of the profiles and relates to the rebound of eastern Australia due to subduction cessation after 100 Ma. Most of the other profiles show the same pattern but with a much smaller knickzones. The different rate at which transient knickzones propagate through the landscape in the model is mainly controlled by catchment drainage area, as expected because the tectonic perturbation in the region is characterized by long wavelengths and small amplitudes [*Whittaker and Boulton*, 2012].

By 60 Ma, most of the catchments on the west side of the range have merged to form larger drainage systems (Figure 11a). This aggregation of smaller catchments into larger ones develops a positive feedback where larger drainages with higher stream power at a given slope undermine and capture an adjacent drainage area [*Oskin and Burbank*, 2007]. Most westward flowing rivers show typical concave upward longitudinal geometries suggesting that these alluvial channels have reached equilibrium. Westward draining

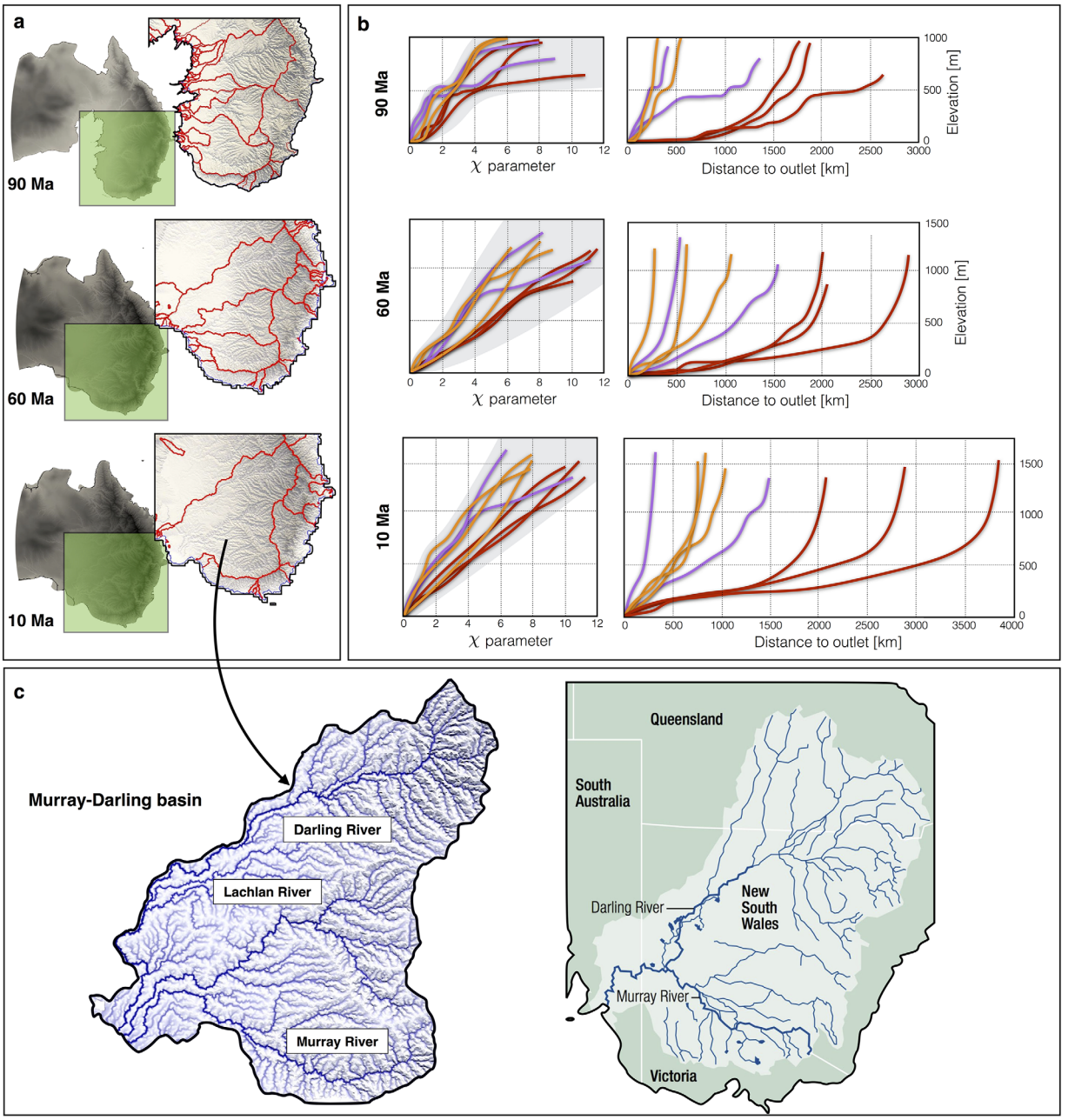

Figure 11. (a) Predicted reorganization of the main southeastern Australia river catchments over the last 90 Myr. (b) Temporal evolution of the parameter χ versus elevation [*Willett et al.*, 2014], and of longitudinal distance versus elevation for three groups of rivers: westward flowing (red), southward flowing (purple) and eastward flowing (orange). (c) Comparison between the predicted (left) and observed [right; *Murray Darling Basin Commission*, 2006] present-day Murray-Darling Basin showing the similarities between simulated and observed drainage systems.

basins are now characterized by graded streams several thousand kilometers long and around 1000 m elevation close to catchment head (Figure 11b—60 Ma), and the χ profiles become more linear. According to *Willett et al.* [2014], for equilibrium to be reached all channel points in both basins should lie on a single linear trend. Here we see that χ values remain discontinuous across the drainage divides, with larger χ for the westward flowing catchments suggesting that the eastern and southern catchments are the aggressors and that the main drainage divide should migrate westward to achieve equilibrium conditions. In our model, this migration is not clearly visible due to constant adjustment of base-level conditions by the combined effect of sea level and tectonic variations. Instead the drainages tend toward equilibrium (linearity of χ profiles) by catchment reorganization.

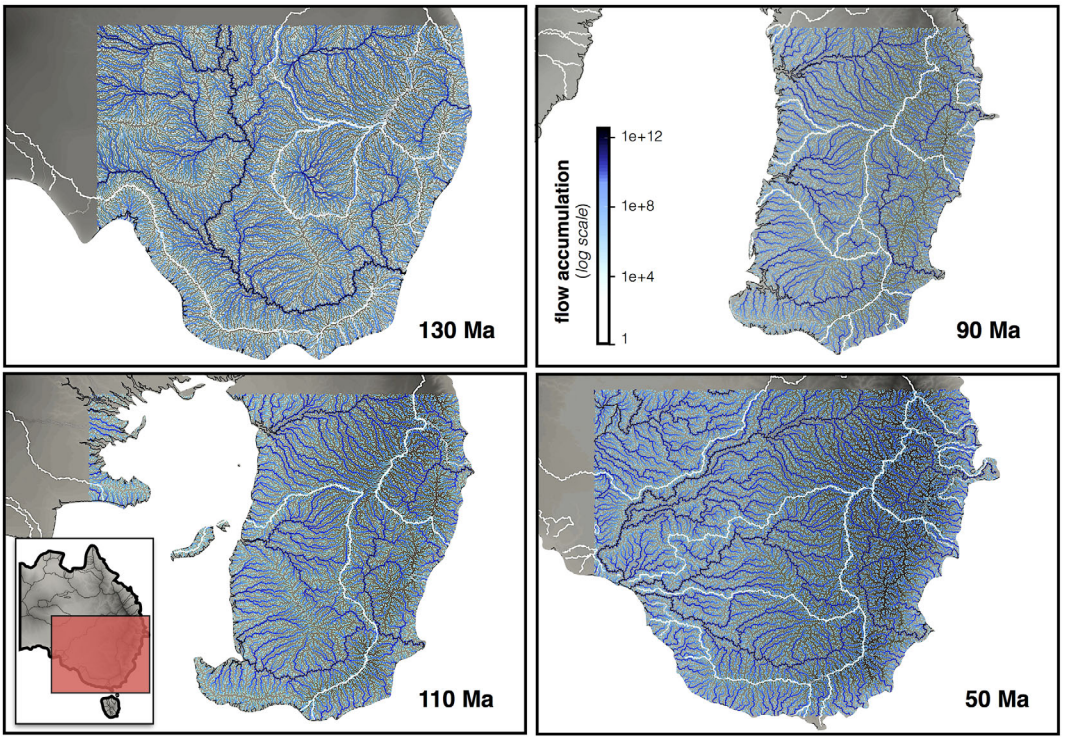

Figure 12. Dynamic temporal reorganization of river networks using the flow accumulation, showing modeled drainage evolution for the southern part of Eastern Australia. White lines show the extent of the main catchment areas for each region.

This reorganization is ongoing over the following 50 million years, with the formation of a large catchment in the western side of the range. The χ profiles gradually become linear over time and the longitudinal river profiles exhibit the same patterns as in Figure 11b—60 Ma. The main differences are in the elevations range (above 1500 m) and overall lengths of the rivers which are directly related to the second phase of uplift induced by the migration of Australia over the edge of the large Pacific mantle upwelling [*Müller et al*., 2016a]. The predicted final main westward draining catchment (Figure 11c) captures the main features of the Murray-Darling basin. This basin drains one seventh of Australian land surface and contains three major rivers: the Murray, Darling and Lachlan Rivers. The extent ($\sim 1.30\times10^6$ km^2), length ($\sim$ 4000 km long) and shape of the simulated basin are well in agreement with the observed ones (i.e., 1.06×10^6 km^2 area and 3375 km length, Figure 11c). Three main rivers could be extracted from the model flow accumulation map. For most of their lengths, as shown in longitudinal river profiles (Figures 8a and 11c—10 Ma), these rivers traverse low-lying land suggesting a low-flow regime. The southeastern rim is the main source of water for these rivers. Their length, position, and profiles seem to be directly comparable with the Darling, Murray, and Lachlan rivers. Keeping in mind the limitations of our model and the crude assumptions on paleogeography, the fidelity of simulated drainage networks with observations [*Murray Darling Basin Commission*, 2006] and the predicted evolution of southeastern catchments [*Lambeck and Stephenson*, 1985; *O'Sullivan et al*., 2000] suggest that dynamic topography played an important role in shaping the geomorphological features and catchment systems of this region.

5.3. Consequences for Dynamic Topography Models and for Continental-Scale Uplift Histories Derived From Present-Day Longitudinal River Profiles

Between 120 and 80 Ma, a total uplift of $\sim$400–600 m is estimated by the mantle flow model (Figure 10d) and correlates with river profiles inversion for the Snowy Mountains, New England, and the Central Highlands suggested by *Czarnota et al*. [2014]. This phase of dynamic uplift is due to the eastward motion of Australia over a sinking slab, first leading to transient subsidence, followed by rebound and uplift as suggested in *Gurnis et al*. [1998] and *Müller et al*. [2016a]. During this period, the landscape

model predicts a phase of drainage reversal (Figure 12) with an important reorganization of the catchment patterns for eastern Australia. By the end of this first phase, the asymmetry between both sides of the Great Dividing Range is in place. The drainage network develops upslope and the highlands are increasingly dissected by tributaries. Rivers flowing westward are characterized by concave-up longer profiles (Figure 11) that develop during the retreat of the epicontinental sea (around 85 Ma).

The northern and southern regions experience different uplift history as discussed in *Müller et al*. [2016a], suggested in *Czarnota et al*. [2014] and shown in Figure 3. This time difference in the second phase of uplift is also expressed on maps of flow accumulation evolution (Figure 12). The northern region (Figure 6) shows a progressive evolution toward equilibrium of the drainage systems between 70 and 50 Ma. During the last 50 Myr, catchment reorganization is still active in the southern eastern region with the formation of a large drainage system similar in shape and size to the Murray-Darling basin [*Murray Darling Basin Commission*, 2006] and (Figure 11c). In this southern region, the distribution of χ shows contrasting values between several drainages sharing a common divide, suggesting that catchments remain in disequilibrium (Figure 11b). This second phase of Cenozoic uplift totaling $\sim$700 m in our model (Figure 10d) is in agreement with river profile inversion model from *Czarnota et al*. [2014] and geological and geomorphological observations [*Holdgate et al*., 1980].

Simulated longitudinal river profiles (Figure 8) present similar shapes and lengths when compared to profiles derived from SRTM data [*Farr et al*., 2007; *Czarnota et al*., 2014]. Large catchments developing on the western side of the Great Dividing Range are also well in agreement with observed ones [*Murray Darling Basin Commission*, 2006; *O'Sullivan et al*., 2000]. It suggests that continental-scale landscape dynamics is strongly controlled by the dynamic topography history in this region. Our approach accounts for the effects of both uplift and subsidence, drainage reorganizations, as well as sea level fluctuations, extending insights from river profile inversion [*Czarnota et al*., 2014]. The landscape evolution model predicts that the main phase of landscape disequilibrium and drainage reorganizations occurred around 130 Ma, with subduction-driven dynamic subsidence controlling the initial organization of the western catchments from 150 to 120 Ma (Figures 3 and 12—130 Ma). It suggests that assuming a constant drainage network may be an acceptable first-order approximation to model past eastern Australian topography from present-day longitudinal river profiles over the last 120 Myr [*Czarnota et al*., 2014]. However, the model predicts that the change from dynamic subsidence to dynamic uplift in the southwest part of the model domain (Figure 3) resulted in large-scale drainage reversal (Figure 12) between 120 and 80 Ma, and in the formation of westward flowing drainages during the retreat of the epicontinental sea between 90 and 80 Ma (Figure 6). This change in drainage direction primarily concerns rivers of the Murray-Darling Basin that do not present major knickzones and therefore have a limited effect on the predicted uplift history of Australia [*Czarnota et al*., 2014]. Inferring past continental-scale uplift histories from the present-day landscape may not be possible back to the Cretaceous for all continents. For instance, mantle flow and surface process models [*Shephard et al*., 2010; *Sacek*, 2014; *Flament et al*., 2015] predict a reversal of the Amazon River from westward-draining to eastward-draining during the Miocene. In such cases, forward methods such as the one present here may be required to unravel past interactions between surface and mantle flow induced processes.

It is worth noting that the model does not take into account regional crustal and lithospheric deformation (thickening or thinning) that would result in tectonic uplift or subsidence. As a consequence, changes in landscape related to tectonic activity in the Flinders Ranges [*Célérier et al*., 2005] and in Victoria [*Wallace et al*., 2005] are not captured by the model. Postrift thermal subsidence [e.g., *McKenzie*, 1978] is also neglected here, and will need to be taken into account to better predict marine sedimentary stratal architectures (Figure 9). In addition, tectonic reconstructions are uncertain and become increasingly uncertain back in geological time [e.g., *Zahirovic et al*., 2015]. The predicted evolution of topography is uncertain both in terms of relative and absolute plate motions as well as plate boundary topologies, which together determine the past location and geometry of subduction zones, and how Australia has moved over over deep-mantle structures through time. The success of the model in predicting the two-stage uplift of Eastern Australia suggests that the tectonic model appropriately captures first-order aspects of past plate motions. However, the predicted epicontinental sea is connected to the open ocean to the south of Australia (Figure 6), whereas the opposite is inferred from paleogeography (Figure 13). This discrepancy could arise from the poorly constrained location, shape or polarity of ill-

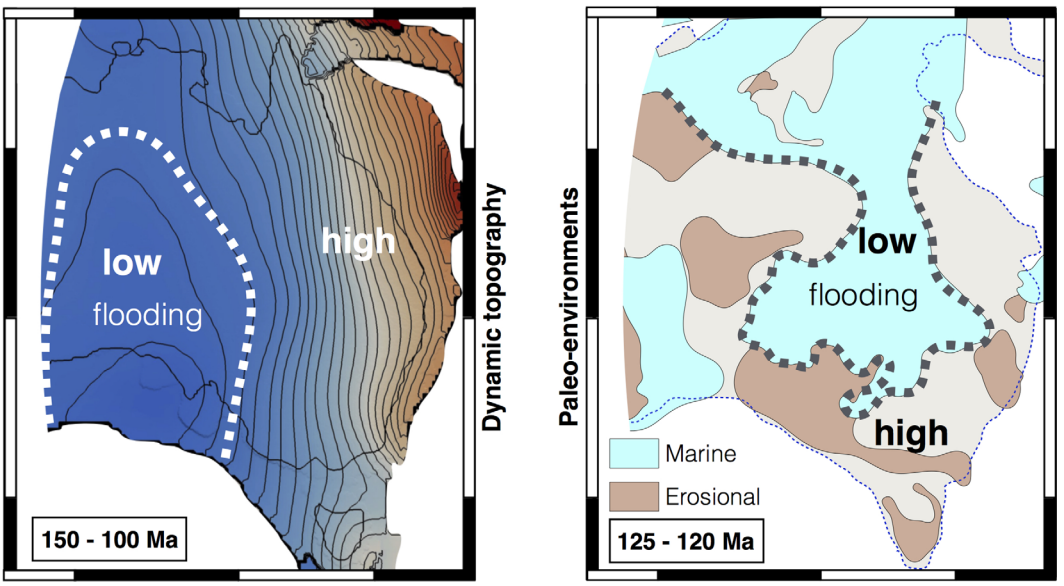

Figure 13. Influence of dynamic topography on the flooding of central Australia and early formation of the eastern Australian highlands. Left: cummulative dynamic topography between 150 and 100 Ma based on *Müller et al.* [2016a] and right: positions of low and high inferred from paleoshorelines and paleoenvironments [*Langford et al.*, 1995].

constrained Cretaceous subduction zones in the Tethys-Pacific junction region [*Seton et al.*, 2012; *Müller et al.*, 2016b], from poorly constrained absolute plate motions between ~150 and 100 Ma, or from a combination of both. Such discrepancies can be addressed in the future either by trial and error using forward models, or ideally using sequential data assimilation, although such methods currently only exist in two dimensions [*Bocher et al.*, 2016].

6. Conclusions

We have coupled the dynamic topography predicted by a paleogeographically constrained mantle flow model to a surface process model to study the evolution of the eastern Australian landscape since the Jurassic Period. We built an initial paleotopography from a global digital elevation model, sediment thickness map and a regional paleoenvironments atlases. Fluvial and hillslope processes simulate landscape dynamics using stream power law and linear diffusion with uniform erodibility and diffusion coefficients. We first designed a series of low-resolution models to test the sensitivity of simulated Australian landscape evolution over the last 150 Myr to input parameters. These models were assessed based on comparisons of simulated elevations with ETOPO5 topography, predicted flooding history of central Australia with paleogeography, and predicted erosion with estimated denudation rates. Using our preferred set of forcing conditions, we then produced a high-resolution model based on a simple history of varying precipitation and long-term sea level. Even though these assumptions limit the predictive power of our results, this coupled approach provides meaningful insights into the fundamental links between continental-scale dynamic topography and landscape evolution. Using temporal and spatial changes in river longitudinal profiles, flow accumulation and χ values, as well as erosion and deposition maps, we show that the motion of the Australian plate over the convecting mantle resulted in significant reorganization of eastern Australia catchments (such as the Murray-Darling basin), including the drainage reversal of the Murray River between ~120 and 100 Ma. Predicted denudation and sedimentation rates are compatible with thermochronology data for the Australian eastern highlands and with cumulative sediment thickness derived from southern Australian offshore basins. In addition, first-order comparisons with observed river profiles and catchment shapes are presented and show that the proposed model is in agreement with present-day observations. The approach could be expanded in the future to investigate long-term sediment transport and provide quantitative constrains on continental-scale sediment routing and basin formation in regions with limited lithospheric deformation.

Acknowledgments
We thank Robert Moucha, Nicky White and an anonymous reviewer for their constructive comments and suggestions which have greatly improve this paper. The authors were supported by ARC grants IH130200012 and DE160101020. This research was undertaken with the assistance of resources from the National Computational Infrastructure (NCI), which is supported by the Australian Government. The results and data presented and discussed here were generated using Badlands model (http://github.com/badlands-model/badlands). Supporting information has been made available through GitHub (http://github.com/badlands-model/g-cubed-2016) and contain all the input and forcing conditions files required to reproduce the experiments published in this article.

References

Altas, I., J. Dym, M. Gupta, and R. P. Manohar (1998), Multigrid solution of automatically generated high-order discretizations for the biharmonic equation, *SIAM J. Sci. Comput.*, *19*, 1575–1585.
Anders, A. M., G. H. Roe, D. R. Montgomery, and B. Hallet (2008), Influence of precipitation phase on the form of mountain ranges, *Geology*, *36*, 479–482.
Artemieva, I. M. (2006), Global thermal model TC1 for the continental lithosphere: Implications for lithosphere secular evolution, *Tectonophysics*, *416*, 245–277.
Austermann, J., and J. X. Mitrovica (2015), Calculating gravitationally self-consistent sea level changes driven by dynamic topography, *Geophys. J. Int.*, *203*, 1909–1922.
Avouac, J. P., and E. B. Burov (1996), Erosion as a driving mechanism of intracontinental mountain growth, *J. Geophys. Res.*, *101*(B8), 17,747–17,769.
Babault, J., et al. (2005), Influence of piedmont sedimentation on erosion dynamics of an uplifting landscape: An experimental approach, *Geology*, *33*(4), 301–304.
Bahr, D. B., E. W. H. Hutton, J. P. M. Syvitski, and L. F. Pratson (2001), Exponential approximations to compacted sediment porosity profiles, *Comput. Geosci.*, *27*(6), 691–700.
Bishop, P. (2007), Long-term landscape evolution: Linking tectonics and surface processes, *Earth Surf. Processes Landforms*, *32*, 329–365.
Bocher, M., N. Coltice, A. Fournier, and P. J. Tackley (2016), A sequential data assimilation approach for the joint reconstruction of mantle convection and surface tectonics, *Geophys. J. Int.*, *204*, 200–214.
Bonnet, S. (2009), Shrinking and splitting of drainage basins in orogenic landscapes from the migration of the main drainage divide, *Nat. Geosci.*, *2*, 766–771.
Bonnet, S., and A. Crave (2003), Landscape response to climate change: Insights from experimental modelling and implications for tectonic versus climatic uplift of topography, *Geology*, *31*, 123–126.
Bower, D. J., M. Gurnis, N. Flament (2015), Assimilating lithosphere and slab history in 4-D Earth models, *Phys. Earth Planet. Inter.*, *238*, 8–22.
Braun, J., and M. Sambridge (1997), Modelling landscape evolution on geological time scales: A new method based on irregular spatial discretization, *Basin Res.*, *9*(1), 27–52.
Braun, J., and S. D. Willett (2013), A very efficient O(n), implicit and parallel method to solve the stream power equation governing fluvial incision and landscape evolution, *Geomorphology*, *180*, 170–179.
Braun, J., A. M. Heimsath, and J. Chappell (2001), Sediment transport mechanisms on soil-mantled hillslopes, *Geology*, *29*(8), 683–686.
Braun, J., X. Robert, and T. Simon-Labric (2013), Eroding dynamic topography, *Geophys. Res. Lett.*, *40*, 1494–1499, doi:10.1002/grl.50310.
Cazenave, A., A. Souriau, and K. Dominh (1989), Global coupling of earth surface topography with hotspots, geoid and mantle heterogeneities, *Nature*, *340*(6228), 54–57.
Célérier, J., M. Sandiford, D. L. Hansen, and M. Quigley (2005), Modes of active intraplate deformation, Flinders Ranges, Australia. *Tectonics*, *24*, TC6006, doi:10.1029/2004TC001679.
Chen, A., J. Darbon, and J. M. Morel (2014), Landscape evolution models: A review of their fundamental equations, *Geomorphology*, *219*, 68–86.
Conrad, C. P., and M. Gurnis (2003), Seismic tomography, surface uplift, and the breakup of Gondwanaland: Integrating mantle convection backwards in time, *Geochem. Geophys. Geosyst.*, *4*(3), 1031, doi:10.1029/2001GC000299.
Czarnota, K., G. Roberts, N. White, and S. Fishwick (2014), Spatial and temporal patterns of Australian dynamic topography from River Profile modelling, *J. Geophys. Res. Solid Earth*, *119*, 1384–1424, doi:10.1002/2013JB010436.
Christie-Blick, N., and N. W. Driscoll (1995), Sequence stratigraphy, *Annu. Rev. Earth Planet. Sci.*, *23*(1), 451–478.
Coulthard, T. J. (2001), Landscape Evolution Models: A software review, *Hydrol. Processes*, *15*, 165–173.
Crave, A., and P. Davy (2001), A stochastic 'precipiton' model for simulating erosion/sedimentation dynamics, *Comput. Geosci.*, *27*, 815–827.
Davy, P., and A. Crave (2000), Upscaling local-scale transport processes in large-scale relief dynamics, *Phys. Chem. Earth*, *25*(6–7), 533–541.
Davy, P., and D. Lague (2009), The erosion/transport equation of landscape evolution models revisited, *J. Geophys. Res.*, *114*, F03007, doi:10.1029/2008JF001146.
Delworth, T., A. J. Broccoli, A. Rosati, R. J. Stouffer, V. Balaji, J. A. Beesley, W. F. Cooke, K. W. Dixon, and J. Dunne (2006), GFDL's CM2 global coupled climate models. Part 1: Formulation and simulation characteristics, *J. Clim.*, *19*(5), 643–74.
Dietrich, W. E., R. Reiss, M. L. Hsu, and D. R. Montgomery (1995), A process-based model for colluvial soil depth and shallow landsliding using digital elevation data, *Hydrol. Processes*, *9*(3–4), 383–400.
Faiz, M., A. Saghafi, N. Sherwood, and I. Wang (2007), The influence of petrological properties and burial history on coal seam methane reservoir characterisation, Sydney Basin, Australia, *Int. J. Coal Geol.*, *70*, 193–208.
Farr, T. G., et al. (2007), The shuttle radar topography mission, *Rev. Geophys.*, *45*, RG2004, doi:10.1029/2005RG000183.
Fernandes, N., and W. E. Dietrich (1997), Hillslope evolution by diffusive processes: The timescale for equilibrium adjustments, *Water Resour. Res.*, *33*(6), 1307–1318.
Flament, N., M. Gurnis, and R. D. Müller (2013), A review of observations and models of dynamic topography, *Lithosphere*, *5*, 189–210.
Flament, N., M. Gurnis, S. Williams, M. Seton, J. Skogseid, C. Heine, and R. D. Müller (2014), Topographic asymmetry of the South Atlantic from global models of mantle flow and lithospheric stretching, *Earth Planet. Sci. Lett.*, *387*, 107–119.
Flament, N., M. Gurnis, R. D. Müller, D. J. Bower, and L. Husson (2015), Influence of subduction history on South American topography, *Earth Planet. Sci. Lett.*, *430*, 9–18.
Forsyth, P. A., and K. R. Vetzal (2002), Quadratic convergence for valuing American options using a penalty method, *SIAM J. Sci. Comput.*, *23*(6), 2095–2122.
Gallagher, K., and K. Lambeck, (1989), Subsidence, sedimentation and sea-level changes in the Eromanga Basin, *Aust. Basin Res.*, *2*, 115–126.
Garcia-Castellanos, D., J. Vergés, J. M. Gaspar-Escribano, and S. Cloetingh (2003), Interplay between tectonics, climate and fluvial transport during the Cenozoic evolution of the Ebro Basin (NE Iberia), *J. Geophys. Res.*, *108*(B7), 2347, doi:10.1029/2002JB002073.
Gasparini, N. M., and M. T. Brandon (2011), A generalized power law approximation for fluvial incision of bedrock channels, *J. Geophys. Res.*, *116*, F02020, doi:10.1029/2009JF001655.
Giachetta, E., N. Gasparini, D. Capolongo, A. Refice, and F. J. Pazzaglia (2012), The role of climate change in drainage network reorganization: Insights from numerical experiments, *EGU Geophys. Res. Abstr.*, *14*, EGU2012-7438.
Goren, L., S. D. Willett, F. Herman, and J. Braun (2014), Coupled numerical-analytical approach to landscape evolution modelling, *Earth Surf. Processes Landforms*, *39*, 522–545.

Gurnis, M., R. D. Müller, and L. Moresi (1998), Cretaceous vertical motion of Australia and the Australian-Antarctic Discordance, *Science*, *279*, 1499–1504.
Gurnis, M., M. Turner, S. Zahirovic, L. DiCaprio, S. Spasojevic, R. D. Müller, J. Boyden, M. Seton, V. C. Manea, and D. J. Bower (2012), Plate tectonic reconstructions with continuously closing plates, *Comput. Geosci.*, *38*, 35–42.
Hager, B. H., and M. A. Richards (1989), Long-wavelength variations in Earth's geoid: Physical models and dynamical implications, *Philos. Trans. R. Soc. A*, *328*(1599), 309–327.
Hallam, A. (1984), Pre-Quaternary sea-level changes, *Annu. Rev. Earth Planet. Sci.*, *12*, 205–243.
Hays, J., and W. Pitman (1973), Lithospheric plate motion, sea level changes and climatic and ecological consequences, *Nature*, *246*, 18–22.
Haq, B. U., and A. M. Al-Qahtani (2005), Phanerozoic cycles of sea-level change on the Arabian Platform, *GeoArabia*, *10*(2), 127–160.
Haq, B. U., J. Hardenbol, and P. R. Vail (1987), Chronology of fluctuating sea levels since the Triassic, *Science*, *235*, 1156–1167.
Heine, C., R. D. Müller, B. Steingberger, and L. DiCaprio (2010), Integrating deep Earth dynamics in paleogeographic reconstructions of Australia, *Tectonophysics*, *483*(1–2), 135–150.
Heine, C., L. G. Yeo, and R. D. Müller (2015), Evaluating global paleoshoreline models for the Cretaceous and Cenozoic, *Aust. J. Earth Sci.*, *62*(3), 275–287, doi:10.1080/08120099.2015.1018321.
Hodgetts, D., S. S. Egan, and G. D. Williams (1998), Flexural modelling of continental lithosphere deformation: A comparison of 2D and 3D techniques, *Tectonophysics*, *294*, 1–20.
Hoggard, M. J., N. White, and D. Al-Attar (2016), Global dynamic topography observations reveal limited influence of large-scale mantle flow, *Nature Geoscience*, *9*, 456–463.
Holdgate, G., M. Wallace, S. Gallagher, B. Wagstaff, and D. Moore (2008), No mountains to snow on: Major post-Eocene uplift of the East Victoria Highlands; evidence from Cenozoic deposits, *Aust. J. Earth Sci.*, *55*, 211–234.
Howard, A. (1980), Thresholds in river regimes, in *Thresholds in Geomorphology*, edited by D. R. Coates and J. D. Vitek, pp. 227–258, George Allen & Unwin, London.
Howard, A. D., and G. Kerby (1983), Channel changes in badlands, *Geol. Soc. Am. Bull.*, *94*, 739–752.
Howard, A. D., W. E. Dietrich, and M. A. Seidl (1994), Modelling fluvial erosion on regional to continental scales, *J. Geophys. Res.*, *99*(B7), 13,971–13,986.
Jennings, J. N., and J. A. Mabbutt (1986), Physiographic outlines and regions, *Australia—A Geography: The Natural Environment*, vol. 1, edited by D. N. Jeans, pp. 80–96, Sydney Univ. Press, Sydney.
Kohn, B. P., A. J. W. Gleadow, R. W. Brown, K. Gallagher, P. B. O'sullivan, and D. A. Foster (2002), Shaping the Australian crust over the last 300 million years: Insights from fission track thermotectonic imaging and denudation studies of key terranes, *Aust. J. Earth Sci.*, *49*, 697–717.
Kohn, B. P., A. J. Gleadow, R. W. Brown, K. Gallagher, M. Lorencak, and W. P. Noble (2005), Visualizing thermotectonic and denudation histories using apatite fission track thermochronology, *Rev. Mineral. Geochem.*, *58*(1), 527–565, doi:10.2138/rmg.2005.58.20.
Kooi, H., and C. Beaumont (1996), Large-scale geomorphology: Classical concepts reconciled and integrated with contemporary ideas via a surface processes model, *J. Geophys. Res.*, *101*(B2), 3361–3386.
Lague, D., A. Crave, and P. Davy (2003), Laboratory experiments simulating the geomorphic response to tectonic uplift, *J. Geophys. Res.*, *108*(B1), 2008, doi:10.1029/2002JB001785.
Lague, D., N. Hovius, and P. Davy (2005), Discharge, discharge variability, and the bedrock channel profile, *J. Geophys. Res.*, *110*, F04006, doi:10.1029/2004JF000259.
Lambeck, K., and R. Stephenson (1985), Post-orogenic evolution of a mountain range: South-eastern Australian highlands, *Geophys. Res. Lett.*, *12*(12), 801–804, doi:10.1029/GL012i012p00801.
Li, F., C. Dyt, and C. Griffiths (2004), 3D modelling of flexural isostatic deformation, *Comput. Geosci.*, *30*(9), 1105–1115.
Lithgow-Bertelloni, C., and M. Gurnis (1997), Cenozoic subsidence and uplift of continents from time-varying dynamic topography, *Geology*, *25*(8), 735–738.
Lloyd, J., A. S. Collins, J. L. Payne, S. Glorie, S. Holford, and A. J. Reid (2015), Tracking the Cretaceous transcontinental Ceduna River through Australia: The hafnium isotope record of detrital zircons from offshore southern Australia, *Geosci. Front.*, *7*, 237–244.
Langford, R., G. Wilford, E. Truswell, and A. Isern (1995), *Paleogeographic Atlas of Australia*, Cainozoic Aust. Geol. Surv. Organ., Canberra, Australia.
Mavromatidis, A. (2006), Burial/exhumation histories for the Cooper Eromanga Basins and implications for hydrocarbon exploration, *East. Aust. Basin Res.*, *18*, 351–373.
McKenzie, D. (1978), Some remarks on the development of sedimentary basins, *Earth Planet. Sci. Lett.*, *40*, 25–32.
Miall, A. D. (1992), Exxon global cycle chart: An event for every occasion?, *Geology*, *20*, 787–790.
Miller, K. G., M. A. Kominz, J. V. Browning, J. D. Wright, G. S. Mountain, M. E. Katz, P. J. Sugarman, B. S. Cramer, N. Christie-Blick, and S. F. Pekar (2005), The Phanerozoic record of global sea-level change, *Science*, *310*, 1293–1298.
Montgomery, D. R. (2001), Slope distributions, threshold hillslopes, and steady-state topography, *Am. J. Sci.*, *301*, 432–454.
Moucha, R., and A. M. Forte (2011), Changes in African topography driven by mantle convection, *Nat. Geosci.*, *4*, 707–712.
Müller, R. D., M. Sdrolias, C. Gaina, B. Steinberger, and C. Heine (2008), Long-term sea-level fluctuations driven by ocean basin dynamics, *Science*, *319*(5868), 1357–1362.
Müller, R. D., N. Flament, K. J. Matthews, S. E. Williams, and M. Gurnis (2016a), Formation of Australian continental margin highlands driven by plate-mantle interaction, *Earth Planet. Sci. Lett.*, *441*, 60–70.
Müller, R. D., et al. (2016b). Ocean basin evolution and global-scale plate reorganization events since Pangea breakup, *Annu. Rev. Earth Planet. Sci.*, *44*, 107–138.
Murray Darling Basin Commission (2006), *Surface Water Resources*, Canberra, Australia.
Myers, T. S., N. J. Tabor, and L. L. Jacobs (2011), Late Jurassic paleoclimate of Central Africa, *Palaeogeogr. Palaeoclimatol. Palaeoecol.*, *311*(1), 111–125.
National Geophysical Data Center (NOAA) (2006), *ETOPO2v2 2-Minute Global Relief*. [Available at http://www.ngdc.noaa.gov/mgg/fliers/06mgg01.html.]
Norvick, M., R. Langford, T. Hashimoto, N. Rollet, K. Higgins, and M. Morse (2008), New insights into the evolution of the Lord Howe Rise (Capel and Faust basins), offshore eastern Australia, from terrane and geophysical data analysis, in *Eastern Australasian Basins Symposium III: Energy Security for the 21st Century*, edited by J. E. Levin, B. E. Bradshaw, and C. Uruski, pp. 291–309, Petrol. Explor. Soc. of Aust., Sydney.
Oilier, C. D. (1982), The Great Escarpment of eastern Australia: Tectonic and geomorphic significance, *J. Geolo. Soc. Aust.*, *29*(1–2), 13–23.

O'Sullivan, P. B., B. P. Kohn, D. Foster, and A. Gleadow (1995), Fission track data from the Bathurst Batholith: Evidence for rapid mid-Cretaceous uplift and erosion within the eastern highlands of Australia, *Aust. J. Earth Sci.*, *42*, 597–607.
O'Sullivan, P. B., D. L. Gibson, and B. P. Kohn (2000), Long-term landscape evolution of the Murray Basin and its eastern margin, New South Wales: Evidence for Missing Middle to Upper Cretaceous Sediments, in *Central West Symposium Cobar, Extended Abstracts*, edited by K. G. McQueen and C. L. Stegman, pp. 69–71, CRC LEME, Perth.
Oskin, M. E., and D. Burbank (2007), Transient landscape evolution of basement-cored uplifts: Example of the Kyrgyz Range, Tian Shan, *J. Geophys. Res.*, *112*, F03S03, doi:10.1029/2006JF000563.
Paola, C., K. Straub, D. Mohrig, and L. Reinhardt (2009), The unreasonable effectiveness of stratigraphic and geomorphic experiments, *Earth Sci. Rev.*, *97*(1–4), 1–43.
Pelletier, J., (2004), Persistent drainage migration in a numerical landscape evolution model, *Geophys. Res. Lett.*, *31*, L20501, doi:10.1029/2004GL020802.
Pelletier, J., (2011), Fluvial and slope-wash erosion of soil-mantled landscapes: Detachment- or transport-limited?, *Earth Surf. Processes Landforms*, *37*(1), 37–51.
Perron, J. T., and L. Royden (2012), An integral approach to bedrock river profile analysis, *Earth Surf. Processes Landforms*, *38*, 570–576.
Perron, J. T., J. W. Kirchner, and W. E. Dietrich (2009), Formation of evenly spaced ridges and valleys, *Nature*, *460*, 502–505.
Roe, G. H., D. R., Montgomery, and B. Hallet (2003), Orographic precipitation and the relief of mountain ranges, *J. Geophys. Res.*, *108*(B6), 2315, doi:10.1029/2001JB001521.
Royden, L., and J. T. Perron (2013), Solutions of the stream power equation and application to the evolution of river longitudinal profiles. *J. Geophys. Res. Earth Surf.*, *118*, 497–518, doi:10.1002/jgrf.20031.
Ruetenik, G. A., R. Moucha, and G. D. Hoke (2016), Landscape response to changes in dynamic topography, *Terra Nova*, *28*, 289–296.
Sacek, V. (2015), Drainage reversal of the Amazon River due to the coupling of surface and lithospheric processes, *Earth Planet. Sci. Lett.*, *401*, 301–312.
Salles, T. (2016), Badlands: A parallel basin and landscape dynamics model, *SoftwareX*, *5*, 195–202, doi:10.1016/j.softx.2016.08.005.
Salles, T., and G. Duclaux (2015), Combined hillslope diffusion and sediment transport simulation applied to landscape dynamics modelling, *Earth Surf. Processes Landforms*, *40*(6), 823–839.
Salles, T., and L. Hardiman (2016), Badlands: An open-source, flexible and parallel framework to study landscape dynamics, *Comput. Geosci.*, *91*, 77–89.
Salles, T., C. Griffiths, C. Dyt, and F. Li (2011), Australian shelf sediment transport responses to climate change-driven ocean perturbations, *Mar. Geol.*, *282*(3–4), 268–274.
Seton, M., et al. (2012), Global continental and ocean basin reconstructions since 200 Ma, *Earth Sci. Rev.*, *113*, 212–270.
Shephard, G. E., R. D. Müller, L. Liu, and M. Gurnis (2010), Miocene drainage reversal of the Amazon River driven by plate-mantle interaction, *Nat. Geosci.*, *3*, 870–875.
Sklar, L. S., and W. E. Dietrich (2006), The role of sediment in controlling steady-state bedrock channel slope: Implications of the saltation-abrasion incision model, *Geomorphology*, *82*, 58–83.
Simoes, M., J. Braun, and S. Bonnet (2010), Continental-scale erosion and transport laws: A new approach to quantitatively investigate macroscale landscapes and associated sediment fluxes over the geological past, *Geochem. Geophys. Geosyst.*, *11*, Q09001, doi:10.1029/2010GC003121.
Simons, F. J., M. T. Zuber, and J. Korenaga (2000), Isostatic response of the Australian lithosphere: Estimation of effective elastic thickness and anisotropy using multitaper spectral analysis, *J. Geophys. Res.*, *105*(B8), 19,163–19,184.
Sklar, L. S., and W. E. Dietrich (1998), River longitudinal profiles and bedrock incision models: Stream power and the influence of sediment supply, *Rivers Over Rock: Fluvial Processes in Bedrock Channels, AGU Geophys. Monogr.*, vol. 107, edited by K. Tinkler and E. E. Wohl, pp. 237–260, AGU, Washington, D. C.
Smithson, P., K. Addison, and K. Atkinson (2008), *Fundamentals of the Physical Environment*, 4th ed., 626 pp., Routledge, London.
Stadler, G., M. Gurnis, C. Burstedde, L. C. Wilcox, L. Alisic, and O. Ghattas (2010), The dynamics of plate tectonics and mantle flow: From local to global scales, *Science*, *329*, 1033–1038.
Swain, C. J., and J. F. Kirby (2006), An effective elastic thickness map of Australia from wavelet transforms of gravity and topography using Forsyth's method, *Geophys. Res. Lett.*, *33*, L02314, doi:10.1029/2005GL025090.
Sweeney, K. E., J. J. Roering, and C. Ellis (2015), Experimental evidence for hillslope control of landscape scale, *Science*, *349*, 51–53.
Tetzlaff, D., and J. Harbaugh (1989), *Simulating Clastic Sedimentation, Comput. Methods Geosci.*, 202 pp., VanNostrand Reinhold, New York.
Tucker, G. E. (2004), Drainage basin sensitivity to tectonic and climatic forcing: Implications of a stochastic model for the role of entrainment and erosion threshold, *Earth Surf. Processes Landforms*, *29*, 185–205.
Tucker, G. E. (2009), Natural experiments in landscape evolution, *Earth Surf. Processes Landforms*, *34*(10), 1450–1460.
Tucker, G. E., and R. L. Slingerland (1997), Drainage basin responses to climate change, *Water Resour. Res.*, *33*(8), 2031–2047.
Tucker, G. E., and R. L. Bras (1998), Hillslope processes, drainage density, and landscape morphology, *Water Resour. Res.*, *34*(10), 2751–2764.
Tucker, G. E., and G. R. Hancock (2010), Modelling landscape evolution, *Earth Surf. Process. Landf.*, *35*(1), 28–50.
Tucker, G. E., S. T. Lancaster, and N. M. Gasparini (2001), The channel-hillslope integrated landscape development (CHILD) model, in *Landscape Erosion and Evolution Modelling*, 3r ed., edited by R. S. Harmon and W. Doe, chap. 12, pp. 349–388, Kluwer Acad./Plenum, New York.
Van Der Meer, D. G., R. E. Zeebe, D. J. J. Van Hinsbergen, A. Sluijs, W. Spakman, and T. H. Torsvik (2014), Plate tectonic controls on atmospheric CO_2 levels since the Triassic, *Proc. Natl. Acad. Sci. U. S. A.*, *111*, 4380–4385.
Veevers, J. J. (1984), *Phanerozoic Earth History of Australia*, Clarendon Press, Oxford.
Veevers, J. J. (1994), Pangea: Evolution of a supercontinent and its consequences for Earth's paleoclimate and sedimentary environments, in *Pangea: Paleoclimate, Tectonics, and Sedimentation During Accretion, Zenith and Breakup of a Supercontinent*, vol. 288, edited by G. D. Klein, pp. 13–23, Spec. Pap. Geol. Soc. of America, Boulder, Colo.
Wallace, M. W., J. A. Dickinson, D. H. Moore, and M. Sandiford (2005), Late Neogene strandlines of southern Victoria: A unique record of eustasy and tectonics in southeast Australia, *Aust. J. Earth Sci.*, *52*, 279–297.
Watts, A. B., and J. Thorne (1984), Tectonics, global changes in sea level and their relationship to stratigraphical sequences at the US Atlantic continental margin, *Mar. Petrol. Geol.*, *1*, 3–19, doi:10.1016/0264-8172(84)90134-X.
Whipple, K. (2009), The influence of climate on the tectonic evolution of mountain belts, *Nat. Geosci.*, *2*, 97–104.
Whipple, K., and G. E. Tucker (1999), Dynamics of the stream-power river incision model: Implications for height limits of mountain ranges, landscape response timescales, and research needs, *J. Geophys. Res.*, *104*(B8), 17,661–17.
Whipple, K. X., and B. J. Meade (2004), Controls on the strength of coupling among climate, erosion, and deformation in two-sided, frictional orogenic wedges at steady state, *J. Geophys. Res.*, *109*, F01011, doi:10.1029/2003JF000019.

Whipple, K. X., and B. J. Meade (2006), Orogen response to changes in climatic and tectonic forcing, *Earth Planet. Sci. Lett.*, *243*, 218–228.
Whittaker, A. C., and S. J. Boulton (2012), Tectonic and climatic controls on knickpoint retreat rates and landscape response times, *J. Geophys. Res.*, *117*, F02024, doi:10.1029/2011JF002157.
Whittaker, J., A. Goncharov, S. Williams, R. D. Müller, and G. Leitchenkov (2013), Global sediment thickness dataset updated for the Australian-Antarctic Southern Ocean, *Geochem. Geophys. Geosyst.*, *14*, 3297–3305, doi:10.1002/ggge.20181.
Wickert, A. D. (2015), Open-source modular solutions for flexural isostasy: gFlex v1.0, *Geosci. Model Dev. Discuss.*, *8*, 4245–4292.
Willett, S. D., S. W. McCoy, J. T. Perron, L. Goren, and C. Y. Chen (2014), Dynamic reorganization of river basins, *Science*, *343*, 1248765.
Willgoose, G. (2005), Mathematical modelling of whole landscape evolution, *Annu. Rev. Earth Planet. Sci.*, *33*(1), 443–459.
Winterbourne, J., N. White, and A. Crosby (2014), Accurate measurements of residual topography from the oceanic realm, *Tectonics*, *33*, 982–1015, doi:10.1002/2013TC003372.
Yang, R., S. D. Willett, and L. Goren (2015), In situ low-relief landscape formation as a result of river network disruption, *Nature*, *520*, 526–529.
Zahirovic, S., R. D. Müller, M., Seton and N. Flament (2015), Tectonic speed limits from plate kinematic reconstructions, *Earth Planet. Sci. Lett.*, *418*, 40–52.
Zhong, S., A. McNamara, E. Tan, L. Moresi, and M. Gurnis (2008), A benchmark study on mantle convection in a 3-D spherical shell using CitcomS, *Geochem. Geophys. Geosyst.*, *9*, Q10017, doi:10.1029/2008GC002048.
Zuber, M. T., T. D. Bechtel, and D. W. Forsyth (1989), Effective elastic thicknesses of the lithosphere and mechanisms of isostatic compensation in Australia, *J. Geophys. Res.*, *94*(B7), 9353–9367.